CANCER

Mitochondrial calcium signaling regulates branched-chain amino acid catabolism in fibrolamellar carcinoma

Nicole M. Marsh[1]†, Melissa J. S. MacEwen[1]†, Jane Chea[1], Heidi L. Kenerson[2], Albert A. Kwong[1], Timothy M. Locke[1], Francisco Javier Miralles[1], Tanmay Sapre[1], Natasha Gozali[3], Madeleine L. Hart[4], Theo K. Bammler[5], James W. MacDonald[5], Lucas B. Sullivan[4], G. Ekin Atilla-Gokcumen[3], Shao-En Ong[1], John D. Scott[1], Raymond S. Yeung[2], Yasemin Sancak[1]*

Metabolic adaptations are essential for survival. The mitochondrial calcium uniporter plays a key role in coordinating metabolic homeostasis by regulating mitochondrial metabolic pathways and calcium signaling. However, a comprehensive analysis of uniporter-regulated mitochondrial pathways has remained unexplored. Here, we investigate consequences of uniporter loss and gain of function using uniporter knockout cells and fibrolamellar carcinoma (FLC), which we demonstrate to have elevated mitochondrial calcium levels. We find that branched-chain amino acid (BCAA) catabolism and the urea cycle are uniporter-regulated pathways. Reduced uniporter function boosts expression of BCAA catabolism genes and the urea cycle enzyme ornithine transcarbamylase. In contrast, high uniporter activity in FLC suppresses their expression. This suppression is mediated by the transcription factor KLF15, a master regulator of liver metabolism. Thus, the uniporter plays a central role in FLC-associated metabolic changes, including hyperammonemia. Our study identifies an important role for the uniporter in metabolic adaptation through transcriptional regulation of metabolism and elucidates its importance for BCAA and ammonia metabolism.

INTRODUCTION

Efficient utilization of energy sources based on their availability and cellular needs requires metabolic flexibility. Mitochondrial calcium (Ca^{2+}) signaling plays a central role in metabolic adaptation to acute or chronic changes in energy demands and metabolite levels (*1–5*). A principal regulator of this signaling pathway is the mitochondrial Ca^{2+} uniporter (hereon referred to as the uniporter), a Ca^{2+}-selective channel in the inner mitochondrial membrane. The uniporter facilitates bulk entry of Ca^{2+} into the mitochondrial matrix (*6, 7*). This Ca^{2+} influx contributes to activation of the tricarboxylic acid (TCA) cycle, buffering of cytosolic Ca^{2+} signaling, or mitochondrial damage and cell death, depending on the amount of Ca^{2+} that enters the mitochondria (*8*). Thus, the uniporter regulates metabolism, mitochondrial and cytosolic Ca^{2+} signaling, and cell survival.

Five core proteins constitute the uniporter: three transmembrane proteins (MCU, EMRE, and MCUb) and two membrane-associated regulatory subunits (MICU1-2) (*6, 7, 9, 10*). MCU and EMRE are necessary and sufficient to form a functional Ca^{2+} channel, and MICU1-2 and MCUb regulate uniporter activity (*10–13*). In addition, diverse physiological and pathological stimuli alter uniporter-mediated mitochondrial Ca^{2+} uptake through transcriptional and posttranslational mechanisms (*1, 8, 14*). Both increased and decreased mitochondrial Ca^{2+} levels are observed in disease-associated states, such as high-fat diet–induced obesity (*15*), neurodegeneration (*16, 17*), metabolic disorders (*18*), and cancer (*19*). Reduced mitochondrial Ca^{2+}

uptake leads to slower cell proliferation rates (*20–22*), reduced body size (*23, 24*), exercise intolerance (*24*), and epigenetic changes (*25*) in mice. Conversely, increased mitochondrial Ca^{2+} load is associated with mitochondrial damage and cell death (*26*). Nevertheless, enhanced uniporter activity is thought to be beneficial during energetic stress (*1*), pointing to a complex regulation of mitochondrial Ca^{2+} signaling in an effort to balance cellular metabolic needs.

Despite the importance of the uniporter for metabolic adaptation, a comprehensive analysis of mitochondrial pathways that are regulated by the uniporter is lacking. To better understand the effects of the uniporter on mitochondrial function, we analyzed MCU knockout (KO) mitochondria using proteomics and RNA sequencing. Our results show increased expression of branched-chain amino acid (BCAA) catabolism proteins in HeLa MCU KO cells. Furthermore, a key phosphorylation event that inhibits pathway activity is reduced in these cells, thereby augmenting BCAA catabolism.

To determine whether these metabolic changes are reversed under conditions of elevated mitochondrial Ca^{2+}, we turned to fibrolamellar carcinoma (FLC), an oncocytic tumor with indications of increased mitochondrial Ca^{2+} levels in the literature (*27–29*). FLC is a rare liver cancer that primarily affects adolescents and young adults. Recent in-depth analyses of the FLC proteomes and transcriptomes identified substantial differences in tumor mitochondria and metabolism compared to those in adjacent non-tumor liver (NTL) samples (*30*). These studies indicate a key role for mitochondria in FLC pathogenesis.

Using patient samples and cell models, we show that increased mitochondrial Ca^{2+} level is a distinguishing feature of FLC. Furthermore, expression of BCAA pathway proteins is attenuated in FLC, a phenotype that is reversed by MCU knockdown (KD). Activation of BCAA catabolism hinders growth in cellular FLC models. We also report that expression of the transcription factor Krüppel-like factor 15 (KLF15), a regulator of multiple BCAA catabolism genes, is regulated by MCU and is suppressed in FLC tumors. This pathologic event has important

[1]Department of Pharmacology, University of Washington, Seattle, WA, USA. [2]Department of Surgery, University of Washington Medical Center, Seattle, WA, USA. [3]Department of Chemistry, University at Buffalo, State University of New York, Buffalo, NY, USA. [4]Human Biology Division, Fred Hutchinson Cancer Center, Seattle, WA, USA. [5]Department of Environmental and Occupational Health Sciences, University of Washington, Seattle, WA, USA.
*Corresponding author. Email: sancak@uw.edu
†These authors contributed equally to this work.

implications for patients with FLC. KLF15 is vital in promoting expression of the urea cycle enzyme ornithine transcarbamylase (OTC) (31). Consequently, down-regulation of OTC may contribute to impaired urea cycle function and subsequently to hyperammonemia and associated encephalopathy diagnosed in some patients with late-stage FLC (32, 33). We observe that, similar to KLF15, OTC expression is suppressed in FLC tumors and is MCU-regulated in cellular models of FLC.

Overall, our results implicate increased uniporter function in FLC and identify BCAA catabolism and the urea cycle as uniporter-regulated pathways downstream of KLF15. On the basis of these findings, we propose that MCU and KLF15 are potential therapeutic targets in the treatment of FLC and its sequelae.

RESULTS

Loss of uniporter slows growth and alters expression of mitochondrial proteins

To better characterize how mitochondria respond to loss of mitochondrial Ca^{2+} uptake, we generated a HeLa MCU KO cell line. In parallel, we generated a rescue cell line by stable expression of FLAG-tagged MCU on the KO background. Loss of MCU reduced cell growth, which was remedied by MCU reexpression (Fig. 1, A and B) (20–22, 34). Although MCU loss is associated with impaired

TCA cycle activity (35), MCU KO cells did not exhibit a notable decrease in their basal respiration, maximal respiration, adenosine 5′-triphosphate (ATP) production–coupled respiration, respiration due to proton leak, or non-mitochondrial oxygen consumption rates (OCRs). In addition, they showed only a mild reduction in their spare respiratory capacity (fig. S1, A to G).

The lack of a severe oxidative phosphorylation defect in MCU KO cells is attributed to the activation of glycolysis and glutamine utilization (20, 34). The contribution of additional metabolic changes that sustain oxidative phosphorylation and energy production in the absence of the uniporter is unclear. To better characterize the effects of MCU loss on the mitochondria, we compared wild-type (WT) and MCU KO mitochondria using proteomics (Fig. 1C) and transcriptomics (Fig. 1D). Gene set enrichment analysis (36) of significantly up-regulated mitochondrial proteins and genes in MCU KO cells showed a strong enrichment of the BCAA catabolism (i.e., Val, Leu, and Ile degradation) pathway and fatty acid oxidation (FAO) pathway in both datasets (fig. S1, H and I). A link between the FAO and MCU has been reported previously (4). We confirmed FAO activation in MCU KO cells by lipid analysis. MCU KO cells contained markedly reduced levels of very long-chain fatty acids compared to WT cells (fig. S1J). This was accompanied by increased levels of acyl-carnitines, fatty acid metabolites that are transported to the mitochondria for oxidation (fig. S1K). Eight of the 48 proteins in the Kyoto
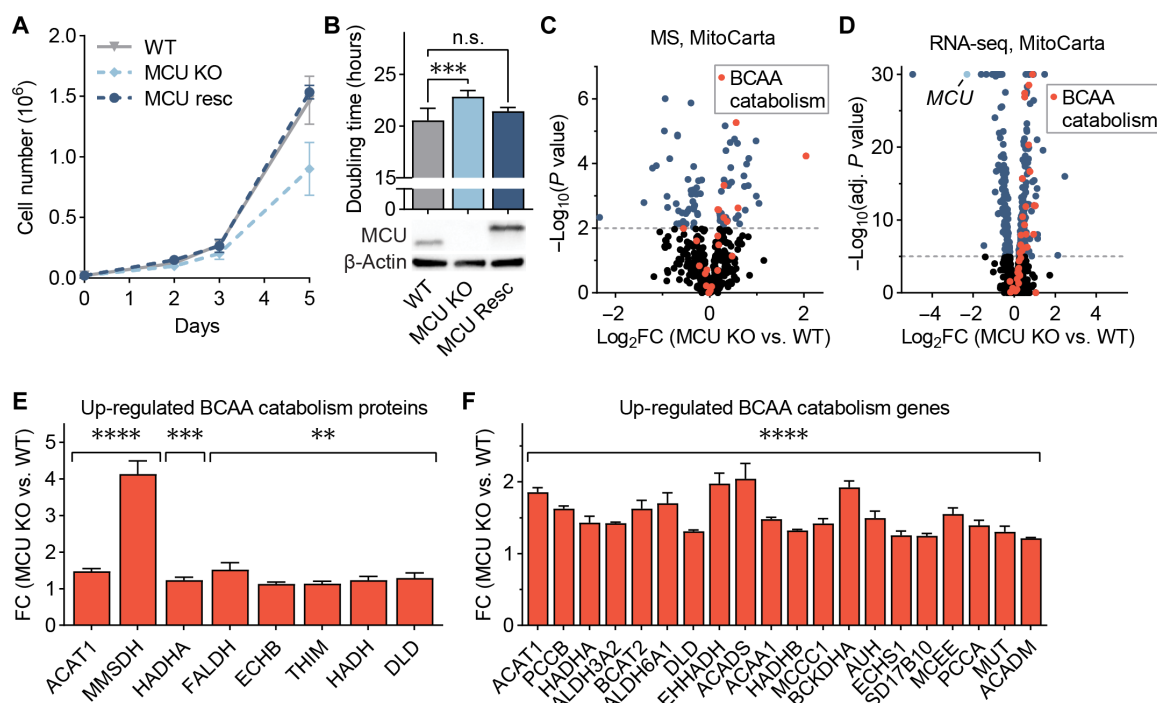

Fig. 1. MCU KO cells exhibit growth defects and altered mitochondrial proteome. (**A**) WT, MCU KO, and MCU rescue (resc) cells were counted on days 2, 3, and 5 after plating; $n = 4$ to 6. (**B**) HeLa cell doubling times were calculated from cell counts on days 2 and 5 in (A); statistical significance was determined by Dunnett's multiple comparisons test following one-way analysis of variance (ANOVA); expression of MCU and MCU-FLAG was confirmed by Western blot. (**C**) Volcano plot shows relative abundance of mitochondrial proteins in MCU KO cells compared to those in WT cells. Red points indicate proteins in the valine, leucine, and isoleucine degradation Kyoto Encyclopedia of Genes and Genomes (KEGG) pathway; $n = 5$. (**D**) Volcano plot shows relative abundance of mRNAs encoding mitochondrial proteins in MCU KO cells compared to those in WT cells. Red points indicate genes in the valine, leucine, and isoleucine degradation KEGG pathway; *MCU* is marked in light blue; $n = 3$. RNA-seq, RNA sequencing. (**E** and **F**) Fold change (FC) of valine, leucine, and isoleucine degradation-associated proteins (E) and genes (F) enriched in MCU KO cells in (C) and (D), respectively; proteins and genes are listed in order of ascending *P* value. All error bars represent SD; n.s., not significant; **$P < 0.01$; ***$P < 0.001$; ****$P < 0.0001$. *n* indicates the number of biological replicates.

Encyclopedia of Genes and Genomes (KEGG) BCAA catabolism pathway (hsa0028) were increased in protein abundance (Fig. 1E). In addition, 20 of the 48 KEGG BCAA catabolism genes showed a 1.3- to 2-fold increase in mRNA levels in MCU KO cells (Fig. 1F). Because of this strong enrichment of BCAA metabolism genes in our dataset and the importance of this process in a diverse set of diseases, we focused on the previously unreported link between mitochondrial calcium signaling and BCAA metabolism.

BCAA catabolism pathway activity is up-regulated by uniporter loss

Next, we monitored expression of select pathway proteins after uniporter perturbation. HeLa cells lacking MCU exhibited no mitochondrial calcium uptake (fig. S2A), and a small but consistent increase in levels of BCAA catabolism proteins (Fig. 2A). We observed similar changes in HeLa cells that lack EMRE, an essential component of the uniporter (Fig. 2B and fig. S2B). To establish whether uniporter-mediated regulation of BCAA catabolism extends to other species and cell types, in particular to cells that originate from tissues with high BCAA catabolism rates such as liver, we blotted for pathway proteins in the mouse hepatocyte cell line AML12 after RNA interference (RNAi)–mediated KD of MCU. MCU KD cells showed reduced mitochondrial calcium uptake rates (fig. S2C) and significantly increased the expression of proteins in the BCAA catabolism pathway (Fig. 2C).

The committed step in the BCAA catabolism pathway is the oxidative decarboxylation reaction carried out by the branched-chain α-ketoacid dehydrogenase (BCKDH) complex. BCKDH activity is regulated by phosphorylation and dephosphorylation of the E1α subunit by the branched-chain α-ketoacid dehydrogenase kinase (BCKDK) and mitochondrial protein phosphatase 1 K (PPM1K), respectively. Phosphorylation by BCKDK is inhibitory, whereas dephosphorylation by PPM1K activates the complex (Fig. 2D). We considered the possibility that BCKD-E1α phosphorylation may be uniporter regulated in a manner similar to the pyruvate dehydrogenase (PDH) complex in some tissues (37, 38). In HeLa cells, BCKD-E1α phosphorylation was significantly reduced in MCU or EMRE KO cells and after MCU KD (Fig. 2, E and F, and fig. S2, D and E). However, in AML12 cells that originate from liver, where PDH phosphorylation is known to be insensitive to mitochondrial Ca^{2+} levels (37), we did not observe a change in phospho-BCKD-E1α (fig. S2F). These data suggest that MCU regulates the activity of the BCAA catabolism pathway both through phosphorylation and transcriptional regulation of pathway enzyme expression in a cell- and tissue-specific manner.

BCAA catabolism helps maintain NADH/NAD$^+$ balance in MCU KO cells

To understand the physiological significance of increased BCAA catabolism in the absence of MCU, we treated cells with the BCKDK inhibitor BT2 and measured cell growth. BT2 treatment (10 μM) of WT and MCU KO cells for 3 days reduced BCKD-E1α phosphorylation in both cell lines (Fig. 3A). WT cell growth was not affected, but MCU KO cells showed increased growth (Fig. 3A). In addition to activating BCAA catabolism, BT2 functions as a mild uncoupler (39). To determine whether the increased growth of MCU KO cells with BT2 treatment was due to mild mitochondrial uncoupling, we treated cells with another mild uncoupler 2,4-dinitrophenol (DNP). DNP treatment did not affect cell growth in WT or MCU KO cells

(fig. S3A). Activation of BCAA catabolism using short hairpin RNA (shRNA)–mediated KD of BCKDK caused a similar increase in the growth of MCU KO cells (fig. S3B). Therefore, we conclude that activation of BCAA catabolism is beneficial for MCU KO cells. To investigate the mechanism of this unexpected growth phenotype, we first considered the possibility that BCAA catabolism supports the TCA cycle, whose activation is impaired in MCU KO cells (1, 24, 34).

Degradation of the three BCAAs—valine, leucine, and isoleucine—generates the TCA cycle metabolites acetyl–coenzyme A (CoA) and succinyl-CoA (Fig. 3B). Loss of MCU abrogates stimulation of the Ca^{2+}-sensitive TCA cycle enzymes PDH, isocitrate dehydrogenase, and oxoglutarate dehydrogenase. This dampens the production of acetyl-CoA and subsequently succinyl-CoA. Thus, we conjectured that increased BCAA catabolism in MCU KO cells supports the TCA cycle. We tested this hypothesis by tracing $^{13}C_6$-labeled leucine carbons after a short labeling period. MCU KO cells had lower levels of total α-ketoglutarate and glutamate (Fig. 3C). Yet, despite having equal amounts of labeled leucine, MCU KO cells showed decreased or unchanged incorporation of leucine-derived carbons into TCA cycle intermediates, as well as into glutamate and aspartate, compared to WT cells (Fig. 3, B and C). These data suggest that BCAA carbons do not preferentially feed into the TCA cycle in MCU KO cells.

As an alternative hypothesis, we speculated that the main role of increased BCAA catabolism in the absence of the uniporter may be to increase reduced form of nicotinamide adenine dinucleotide (oxidized form) (NAD$^+$) (NADH) production independently of the TCA cycle, which is impaired in MCU KO cells (24). To understand the contribution of the BCAA catabolism pathway to NADH/NAD$^+$ homeostasis in MCU KO cells, we starved WT and MCU KO cells of BCAAs for 3 hours and measured relative NADH/NAD$^+$ ratios. As expected, MCU KO cells had a lower NADH/NAD$^+$ ratio than WT cells under normal growth conditions (1, 34). BCAA withdrawal did not affect the NADH/NAD$^+$ ratio in WT cells, whereas MCU KO cells showed a reduction (Fig. 3D). These results indicated that MCU KO cells depend on BCAAs to maintain the NADH/NAD$^+$ ratio and may show sensitivity to BCAA limitation. To test this prediction, we cultured cells in medium with 30% of normal BCAA concentrations, which brings BCAA levels closer to average blood concentrations (fig. S3C) (40). Under these conditions, growth of WT cells was not affected, but MCU KO cells showed a reduction in cell numbers (fig. S3D). These results reveal an unexpected function of BCAA catabolism in cellular energy homeostasis through NADH production independent of the TCA cycle activity and define an important role for Ca^{2+} signaling in this regulation.

Increased mitochondrial Ca^{2+} levels are a hallmark of FLC

FLC is a rare liver cancer that affects children and young adults. This cancer is characterized by a somatic ~400-kb genomic deletion that fuses the first exon of the DnaJ homolog subfamily B member 1 gene (*DNAJB1*) to exons 2 to 10 of the cyclic adenosine 3′,5′-monophosphate–dependent protein kinase catalytic subunit alpha gene (*PRKACA*) (41) (Fig. 4A). This deletion event generates a fusion kinase, DNAJ-PKAc (DP), which we refer to as DP from hereon. FLC tumors are oncocytic neoplasms that are characterized by an aberrant number of mitochondria (27, 28, 42). In addition, earlier reports noted the presence of electron dense particles by electron microscopy (EM) of FLC tumors (28). These electron dense particles are Ca^{2+} phosphate precipitates that form in the mitochondrial matrix (43, 44) as a result of high matrix Ca^{2+} levels.
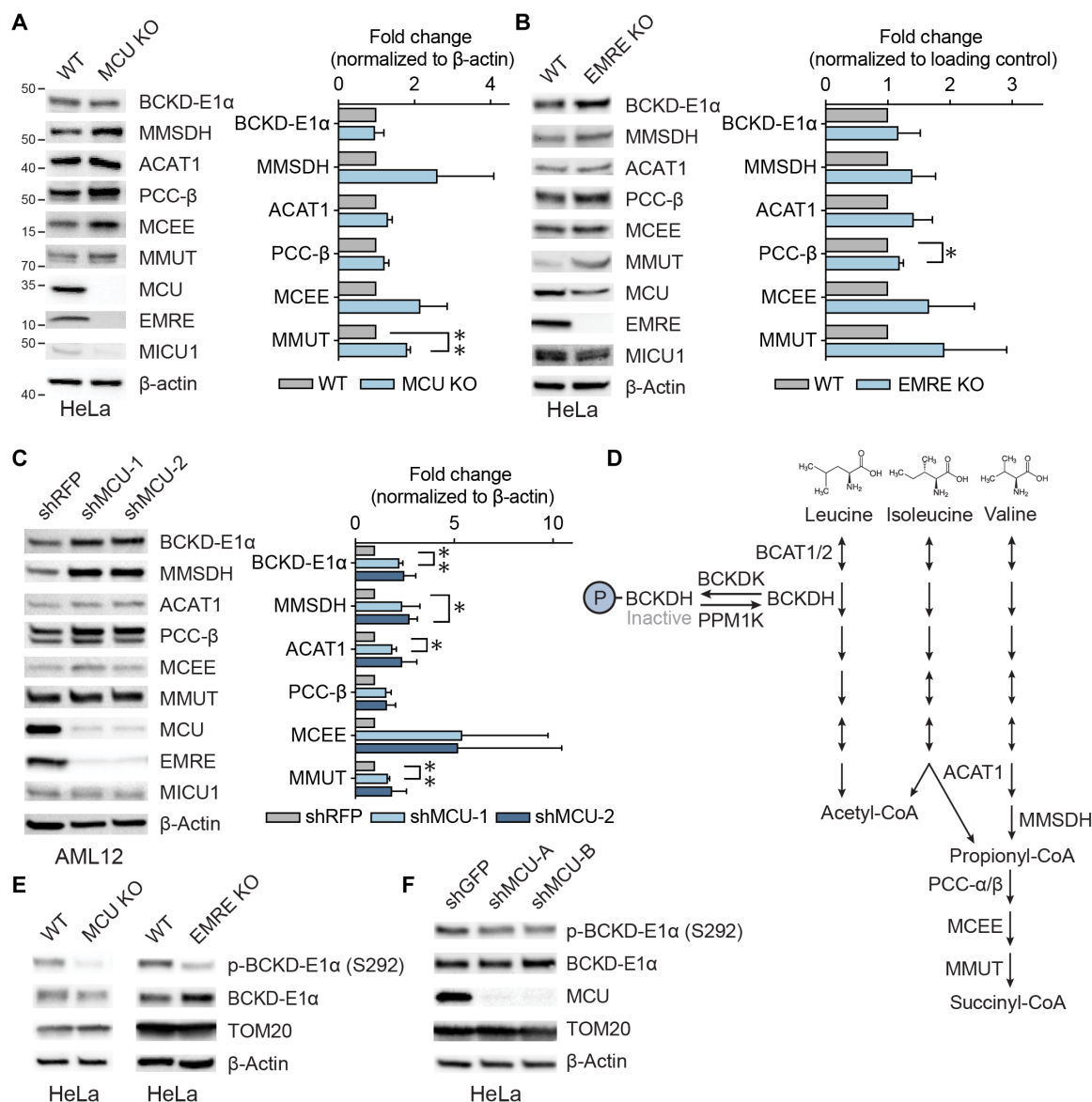
Fig. 2. Mitochondrial calcium uniporter regulates BCAA catabolism pathway. (**A**) Representative immunoblots of select BCAA catabolism proteins and uniporter components and their quantification in HeLa WT and MCU KO cells; $n = 3$. (**B**) Representative immunoblots of select BCAA catabolism pathway proteins and their quantification in HeLa WT and EMRE KO cells; $n = 3$. (**C**) Representative immunoblots of select BCAA pathway proteins and their quantification in AML12 cells following shRNA-mediated MCU KD; $n = 3$. (**D**) Schematic of BCAA catabolism pathway. The committed step in the pathway is catalyzed by the BCKDH complex which is active in the dephosphorylated state. (**E**) Representative immunoblots of phosphorylated and total BCKD-E1α in HeLa WT, MCU KO and EMRE KO cells. (**F**) Representative immunoblots of phosphorylated and total BCKD-E1α after MCU knockdown in HeLa cells. Statistical significance in (A) to (C) was determined by one-sample t test. All error bars represent SD; *P < 0.05; **P < 0.01. n indicates number of biological replicates.

We sought to further characterize mitochondrial Ca^{2+} changes and investigate uniporter function and BCAA metabolism in FLC. We obtained paired FLC and NTL tissue samples from five patients and confirmed DP expression in the tumors using Western blotting with an antibody that detects PKAc (Fig. 4B and table S1). To investigate mitochondrial Ca^{2+} levels in FLC, we performed EM analysis on tumor and NTL from one patient (Fig. 4, C and D). Thirty-nine percent of FLC mitochondria contained one or more electron dense Ca^{2+} deposits compared to 4% of mitochondria from NTL (Fig. 4E). We also analyzed mitochondria from a second patient, for which a control liver sample did not exist, by comparing mitochondria in oncocytic

and peri-oncocytic cells from the tumor periphery (fig. S4, A to C). This sample also showed an increased percentage of mitochondria with electron dense particles in oncocytic cells (24%) compared to that in peri-oncocytic cells (10%) (fig. S4D). EM analysis of tumor and control liver from a patient with hepatocellular carcinoma (HCC) did not show more abundant Ca^{2+} deposits in HCC mitochondria (fig. S4, E to G). These observations suggest that high levels of mitochondrial Ca^{2+} deposits may be an FLC-specific phenotype.

We next quantified levels of the uniporter proteins MCU, EMRE, and MICU1 in FLC and paired NTL control lysates. MCU and EMRE levels were significantly increased relative to TOM20, and
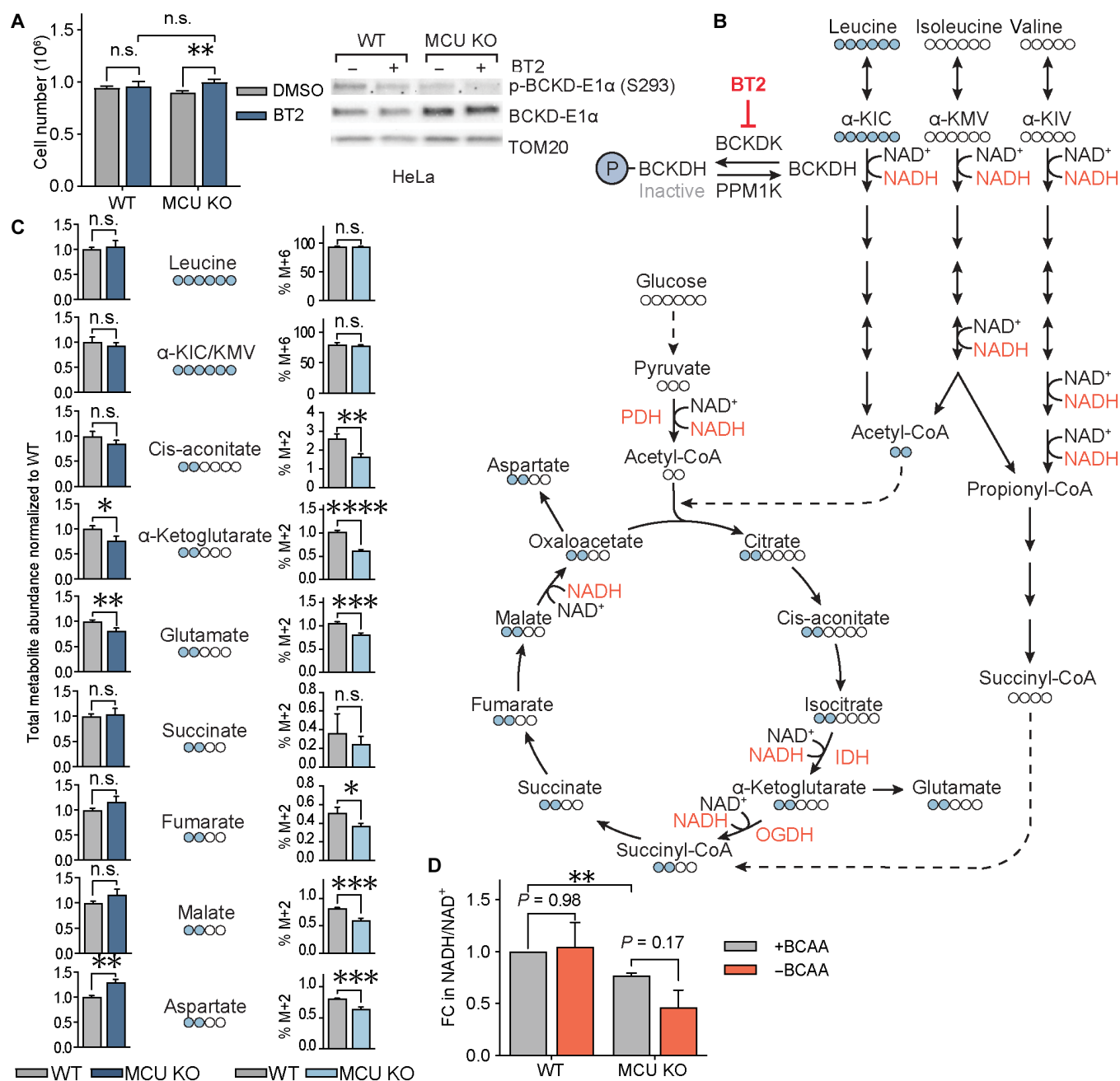
Fig. 3. BCAA catabolism maintains NADH/NAD+ balance in MCU KO cells. (**A**) Cell numbers of WT and MCU KO cells with and without pharmacological activation of BCAA catabolism by BT2. Cells were counted 3 days after plating and treatment; $n = 4$ to 5. Immunoblots show phosphorylated and total BCKD-E1α after vehicle dimethyl sulfoxide (DMSO) or BT2 treatment. Statistical significance was determined by Dunnett's multiple comparisons test following one-way ANOVA. (**B**) Schematic of BCAA catabolism and TCA cycle enzymes and metabolites; BCAA catabolism produces acetyl–coenzyme A (CoA) and succinyl-CoA, which can enter the TCA cycle; Ca2+-regulated enzymes and NAD+/NADH-coupled reactions are shown in red. Labeled leucine carbons (indicated as blue circles) and their incorporation into the TCA cycle are also shown. (**C**) Total abundance of indicated metabolites, including all isotopologs, relative to WT cells (left) and fractional isotopolog abundance for leucine catabolism-relevant isotopologs (right) from WT and MCU KO HeLa cells cultured in $^{13}C_6$-labeled leucine for 2 hours; M+2 and M+6 indicate metabolites with 2 or 6 heavy carbons, respectively. (**D**) Relative NADH/NAD+ ratios in WT and MCU KO cells with and without 3 hours of BCAA starvation are shown. Statistical significance was determined by the Tukey-Kramer test following one-way ANOVA; $n = 3$. All error bars indicate SD; n.s., not significant; *$P < 0.05$; **$P < 0.01$; ***$P < 0.001$; ****$P < 0.0001$. n indicates number of biological replicates.
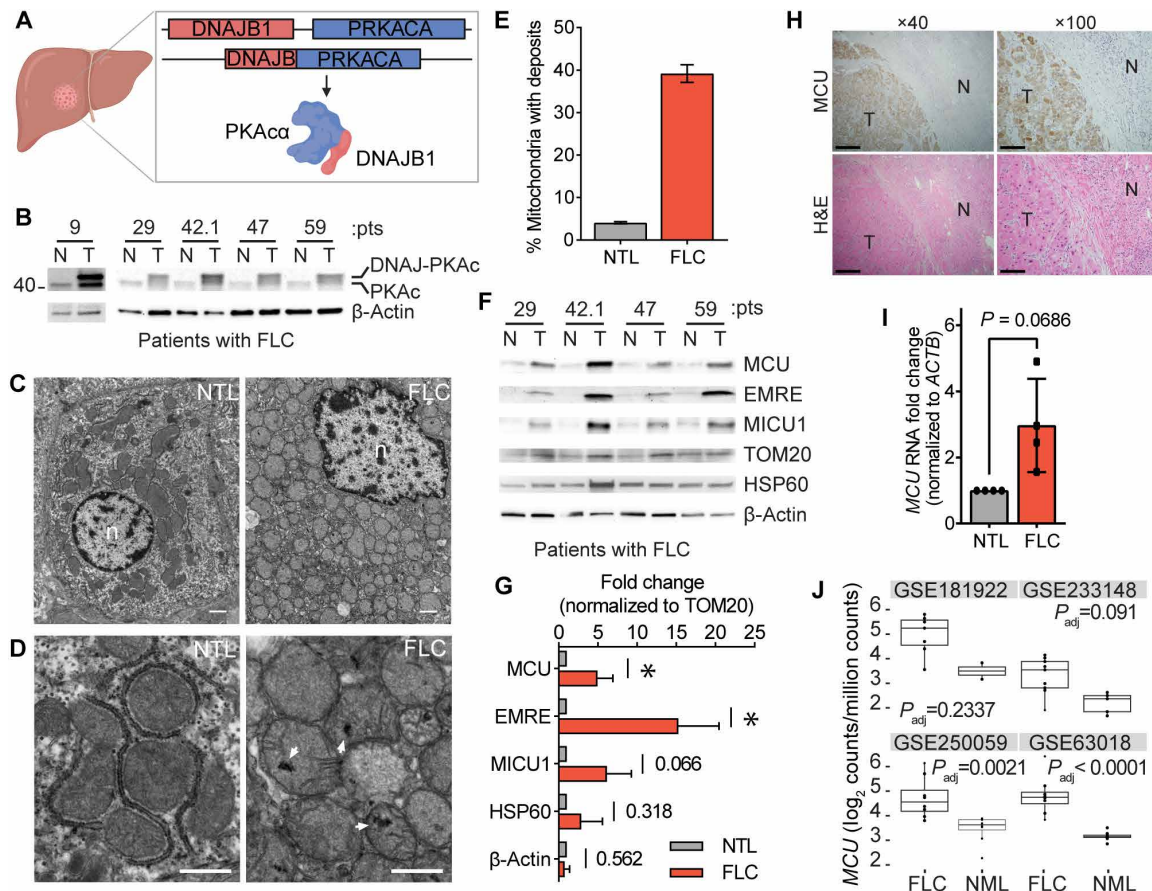
Fig. 4. FLC is characterized by increased mitochondrial Ca^{2+} levels and uniporter expression. (**A**) Schematic of FLC liver tumor with heterozygous deletion in chromosome 19 producing the DNAJ-PKAc (DP) fusion protein. This schematic was created in BioRender (N. Marsh, 2025; https://BioRender.com/up42cz5. (**B**) Immunoblots of lysates from non-tumor (N) and tumor (T) liver from patients with FLC show DP fusion protein expression in the tumor. (**C**) Electron micrographs at ×10,000 magnification of non-tumor (NTL) and tumor (FLC) sections from patient 9; nuclei are labeled n; scale bars, 1 μm. (**D**) Micrographs of samples shown in (C) at ×25,000 magnification; white arrowheads mark representative Ca^{2+} deposits in the tumor; scale bars, 600 nm. (**E**) Percentage of mitochondria from FLC patient 9 with Ca^{2+} deposits; the mean is reported from manual counting of >500 mitochondria per sample by two independent, blinded analysts. (**F**) Immunoblots of uniporter components and control mitochondrial proteins from paired non-tumor (N) and FLC tumor (T) samples. (**G**) Pooled quantification of immunoblots in (F) normalized to TOM20 levels; statistical significance was determined by one-sample t test. (**H**) Hematoxylin and eosin (H&E) and MCU immunohistochemistry (IHC) staining of non-tumor (N) and tumor (T) regions of liver from FLC patient 9; ×40 and ×100 image scale bars are 500 and 200 μm, respectively. (**I**) qPCR analysis of *MCU* RNA expression in paired NTL and tumors from FLC patients 29, 42.1, 47, and 59. (**J**) *MCU* transcript expression in indicated datasets in tumor (FLC) and normal liver (NML). All error bars indicate SD; numbers above error bars indicate *P* values; *$P < 0.05$.

MICU1 trended toward higher expression in tumors (Fig. 4, F and G). The control mitochondrial heat shock protein 60 (HSP60) did not show a significant difference between tumors and control lysates, suggesting that the increase in uniporter protein expression is specific and is not simply a result of increased mitochondrial proteome abundance in FLC. Immunohistochemistry (IHC) analysis of tumor and NTL sections also showed stronger MCU staining in the tumor (Fig. 4H). Quantitative polymerase chain reaction (qPCR) analysis showed that FLC tumors had elevated MCU mRNA levels (Fig. 4I). Analysis of MCU transcript levels in publicly available datasets showed increased MCU expression in FLC tumors compared to that in normal liver (Fig. 4J). These data are consistent with higher uniporter expression driving increased mitochondrial Ca^{2+} levels in FLC.

Cellular FLC models show increased mitochondrial Ca^{2+} levels

To better understand the role of mitochondrial Ca^{2+} signaling in FLC metabolism, we turned to two clonal AML12 cell lines, c14 and c4,

which were previously generated using genome editing (*45*) and used as cellular models of FLC. These clones carry the heterozygous FLC deletion, express a single allele of the fusion kinase DP, and grow faster than WT AML12 cells (Fig. 5, A and B). The clonal cells also recapitulate FLC-associated signaling events and have been successfully used to investigate FLC biology and therapeutics (*45*, *46*).

To determine whether c14 and c4 clones have increased mitochondrial Ca^{2+} levels, we treated digitonin-permeabilized cells with the mitochondrial uncoupler CCCP, which results in release of Ca^{2+} ions from mitochondria. Both clones showed increased mitochondrial Ca^{2+} release compared to WT (Fig. 5C). Measurement of free matrix Ca^{2+} levels using the mitochondria-targeted G-GECO Ca^{2+} reporter (*47*) indicated higher resting Ca^{2+} levels in the FLC clones (Fig. 5, D and E). Resting cytosolic Ca^{2+} levels were similar in the clones and WT cells (fig. S5A). We also measured mitochondrial Ca^{2+} uptake rates in digitonin-permeabilized cells. C14 and c4 cells showed decreased mitochondrial Ca^{2+} uptake rates (Fig. 5, F and G), despite expressing MCU at comparable levels to WT cells (Fig. 5J).
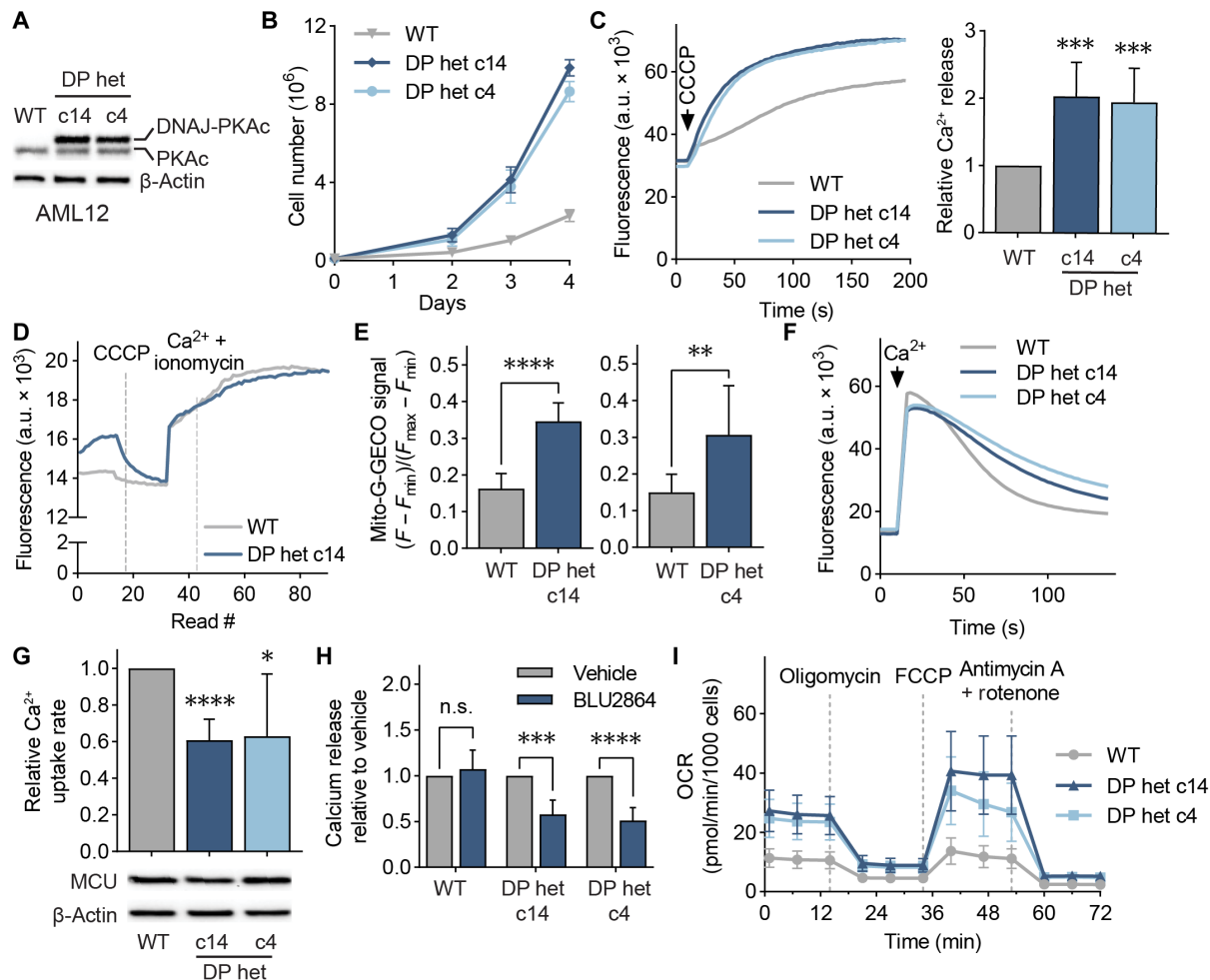
Fig. 5. Cellular models of FLC show DP-dependent increase in mitochondrial Ca^{2+} levels. (**A**) Immunoblot of lysates from WT and FLC clones c14 and c4 using an antibody against PKAc. (**B**) Proliferation curves of cellular models of FLC compared to those of WT AML12 cells; cells were counted on days 2, 3, and 4 after plating; $n = 3$. (**C**) Representative traces and quantification of mitochondrial Ca^{2+} released after CCCP addition in AML12 cells; statistical significance was determined by one-sample t test; $n = 3$. (**D**) Representative trace of mitochondrial free Ca^{2+} levels of AML12 WT and c14 cells quantified using matrix-targeted Ca^{2+} reporter G-GECO (mito-G-GECO). (**E**) Baseline mito-G-GECO fluorescence normalized to minimum and maximum signals in AML12 cells; statistical significance was determined by Mann-Whitney test; $n = 3$ (**F and G**) Representative traces (F) and mitochondrial Ca^{2+} uptake rates (G) in AML12 cells; mitochondrial Ca^{2+} uptake rates were calculated by monitoring Ca^{2+} clearance in the presence of a Ca^{2+} indicator dye; statistical significance was determined by one-sample t test; $n = 3$. Immunoblot of MCU in FLC clones compared to that in WT controls. (**H**) Mitochondrial Ca^{2+} release was assayed as in (C) after cells were treated with 5 μM PKA inhibitor BLU2864 or DMSO for 4 days. Ca^{2+} release was normalized to total protein levels; fold change in released Ca^{2+} is shown relative to DMSO control for each cell line; statistical significance was determined by paired t test, $n = 3$. (**I**) Seahorse extracellular flux analysis of OCRs in FLC clones compared to those in WT AML12 cells at baseline and after indicated treatments; $n = 2$ (five to eight technical replicates each). All error bars indicate SD; n.s., not significant; *$P < 0.05$; **$P < 0.01$; ***$P < 0.001$; ****$P < 0.0001$. n indicates the number of biological replicates.

This decrease in Ca^{2+} uptake rate was not due to reduced mitochondrial membrane potential in FLC clones (fig. S5B) and is likely due to higher concentrations of Ca^{2+} in the matrix negatively affecting mitochondrial Ca^{2+} uptake rates. Next, we tested whether elevated mitochondrial Ca^{2+} levels in c14 and c4 cells are dependent on the kinase activity of DP, the fusion protein that sustains FLC tumor growth (48, 49). The PKA inhibitor BLU2864 (50) did not affect the amount of Ca^{2+} released from WT mitochondria but caused a significant reduction in the FLC clones (Fig. 5H), with concomitant decreases in PKA substrate phosphorylation in all cell lines (fig. S5C).

To investigate the consequences of increased mitochondrial Ca^{2+} levels for oxidative phosphorylation and energy production in FLC, we measured the OCR of AML12 cells with the Seahorse extracellular

flux analyzer. FLC clones showed increased basal, maximal, and non-mitochondrial OCR, as well as increased spare respiratory capacity and proton leak- and ATP production-coupled respiration (Fig. 5I and fig. S5, D to I), as would be expected with increased uniporter function (20, 51). On the basis of our data, we conclude that high mitochondrial Ca^{2+} is a previously underappreciated feature of FLC that is coupled to oncogenic driver DP activity and alters FLC metabolism.

Uniporter regulates expression of proteins involved in BCAA catabolism in FLC

Decreased BCAA catabolism is associated with poor patient outcomes in HCC (52). Yet, the mechanisms by which cancer cells down-regulate

this pathway are not known. We asked whether increased uniporter activity in FLC suppresses expression of BCAA catabolism genes as opposed to the increase that we observed in MCU KO cells. We first analyzed four publicly available FLC gene expression datasets for changes in the BCAA catabolism pathway (GO:0009083), focusing on primary tumor and normal liver. Fifteen of 22 genes in the pathway showed lower expression in FLC compared to that in normal liver (Fig. 6A). Western blot analysis of tumors from patients with FLC also showed significantly reduced levels of BCAA catabolism pathway enzymes compared to that of matching NTL samples, with less than 50% expression in the tumors compared to that in NTL when protein levels were normalized to the outer mitochondrial membrane protein TOM20 (Fig. 6B). These trends were also evident in FLC clones c14 and c4 (Fig. 6C). KD of MCU using two independent shRNAs in FLC cellular models increased expression of BCAA catabolism pathway enzymes (Fig. 6D). Similar to AML12 cells, we did not observe a change in phosphorylation of BCKD-E1α in patient lysates (fig. S6). This suggests that mitochondrial Ca^{2+} signaling regulates the pathway's activity through its effects on protein levels in the liver, in contrast to phospho-regulation observed in HeLa cells. Our results are consistent with previous reports (53) and reflect tissue-specific differences in regulation of mitochondrial metabolism by Ca^{2+} signaling.

To understand the functional significance of BCAA catabolism suppression in FLC, we sought to activate this pathway in AML12 cells. However, murine hepatocytes, unlike human hepatocytes, lack branched-chain amino acid aminotransferase (BCAT) activity, the first enzyme in the BCAA catabolism pathway (54). To overcome this deficit, we expressed BCAT2 in WT and c14 cells and assessed growth in 100, 50, and 30% BCAA-containing medium. In 100% BCAA-containing medium, BCAT2 expression did not significantly affect growth in either cell line. In medium with 50 or 30% BCAA levels, BCAT2 expression did not affect growth of WT cells, but it caused a significant reduction in c14 cells (Fig. 6E). To test the effects of BCAA pathway activation in a human-derived disease model, we determined the effects of BT2-mediated activation of BCAA catabolism on the growth of a patient-derived FLC cell line (FLX1) (55) (Fig. 6F). BT2 treatment of FLX1 cells caused a small but significant growth reduction in 30% BCAA medium. This growth reduction was dependent on PKA kinase activity and was rescued by treatment of cells with PKA inhibitor BLU2468 (Fig. 6F). Overall, these results establish the importance of MCU-mediated BCAA catabolism regulation in FLC metabolic adaptations and oncogene-dependent growth.

Mitochondrial Ca^{2+} signaling regulates expression of KLF15 and its targets in FLC

Reduced mRNA expression of BCAA catabolism pathway enzymes in FLC suggested the presence of a transcriptional regulatory mechanism. KLF15 is a key transcriptional regulator of metabolic gene expression in the liver, including BCAA catabolism and urea cycle genes (31, 56, 57). To investigate whether KLF15 plays a role in FLC metabolism, we initially probed for KLF15 in lysates from patients with FLC by Western blot. FLC tumors exhibited markedly reduced levels of KLF15 (Fig. 7A). IHC of tissue sections from patients with FLC confirmed low KLF15 and high MCU expression in the tumors relative to NTL (Fig. 7B). Likewise, immunoblot analysis demonstrated that KLF15 expression was reduced in AML12 clones c14 and c4 compared to that in WT cells (Fig. 7C).

To investigate the role of uniporter function in KLF15 regulation, we knocked down MCU in AML12 WT and c14 cells. This caused a substantial increase in KLF15 levels (Fig. 7D), suggesting that mitochondrial Ca^{2+} signaling negatively regulates KLF15 expression. We reasoned that reduced KLF15 expression may have important metabolic consequences beyond inhibition of BCAA catabolism in FLC, including regulation of the urea cycle. Defects in the urea cycle can lead to accumulation of ammonia and cause hyperammonemia (Fig. 7E), which can cause neurological damage and death (58). Decreased OTC expression has also been identified as a potential cause of hyperammonemia in some patients with FLC (30). KLF15 KO mice suffer from increased blood ammonia levels due to substantially reduced OTC expression and activity in the liver (31). RNA (Fig. 7, F and G) and protein (Fig. 7H) levels of OTC showed a significant reduction in tumor samples compared to controls, consistent with transcriptional regulation of OTC in FLC. Moreover, KD of MCU in WT AML12 and c14 cells increased OTC expression (Fig. 7I), suggesting a previously unknown link between mitochondrial Ca^{2+} signaling and urea cycle regulation.

On the basis of our data, we propose a model in which mitochondrial Ca^{2+} signaling regulates the BCAA catabolism pathway and the urea cycle through the transcription factor KLF15 in the liver (Fig. 8). In cells with increased mitochondrial Ca^{2+} levels, such as FLC cells, reduced KLF15 expression leads to reduced expression of BCAA catabolism pathway genes, which conserves essential BCAAs for protein synthesis and promotes cell growth. In cells that do not have bulk mitochondrial Ca^{2+} uptake (MCU-deficient cells), increased KLF15 and activated BCAA catabolism supplies the cells with NADH as a compensatory mechanism in the absence of Ca^{2+} stimulation of TCA enzymes.

DISCUSSION

The BCAA catabolism pathway is responsive to nutrients, hormones, and circadian rhythm. Flux through this pathway is altered in disease states including type II diabetes, cardiovascular disease, liver disease, and cancer (59–61). Here, we identify mitochondrial Ca^{2+} signaling as a previously unrecognized mechanism by which the BCAA catabolism pathway is regulated. More specifically, we demonstrate that loss of uniporter function results in increased expression of BCAA catabolism enzymes and activation of the pathway's committed step. Conversely, increased mitochondrial Ca^{2+} uptake inhibits BCAA catabolism transcriptionally. On the basis of our findings, we propose that mitochondrial Ca^{2+} signaling acts as a regulatory switch through which BCAAs are either broken down to support cellular NADH/NAD^+ balance or conserved for translation in accordance with the cell's needs (Fig. 8).

Our findings have additional implications for understanding FLC pathology. First, we show that increased mitochondrial calcium levels are linked to kinase activity of the oncogene DP in this cancer. Second, reduced expression of the KLF15 target OTC is thought to contribute to hyperammonemia observed in patients with FLC (30, 33). Moreover, accumulation of the OTC substrates ammonia and ornithine can support the production of collagen (62–64), which is a large component of the fibrous bands that are hallmarks of FLC tumors. Elevated levels of MCU and down-regulation of KLF15 are associated with increased collagen production and fibrosis in various tissues, supporting a role for this pathway in FLC fibrosis (65–68). Although the mechanism of DP-induced increase in mitochondrial
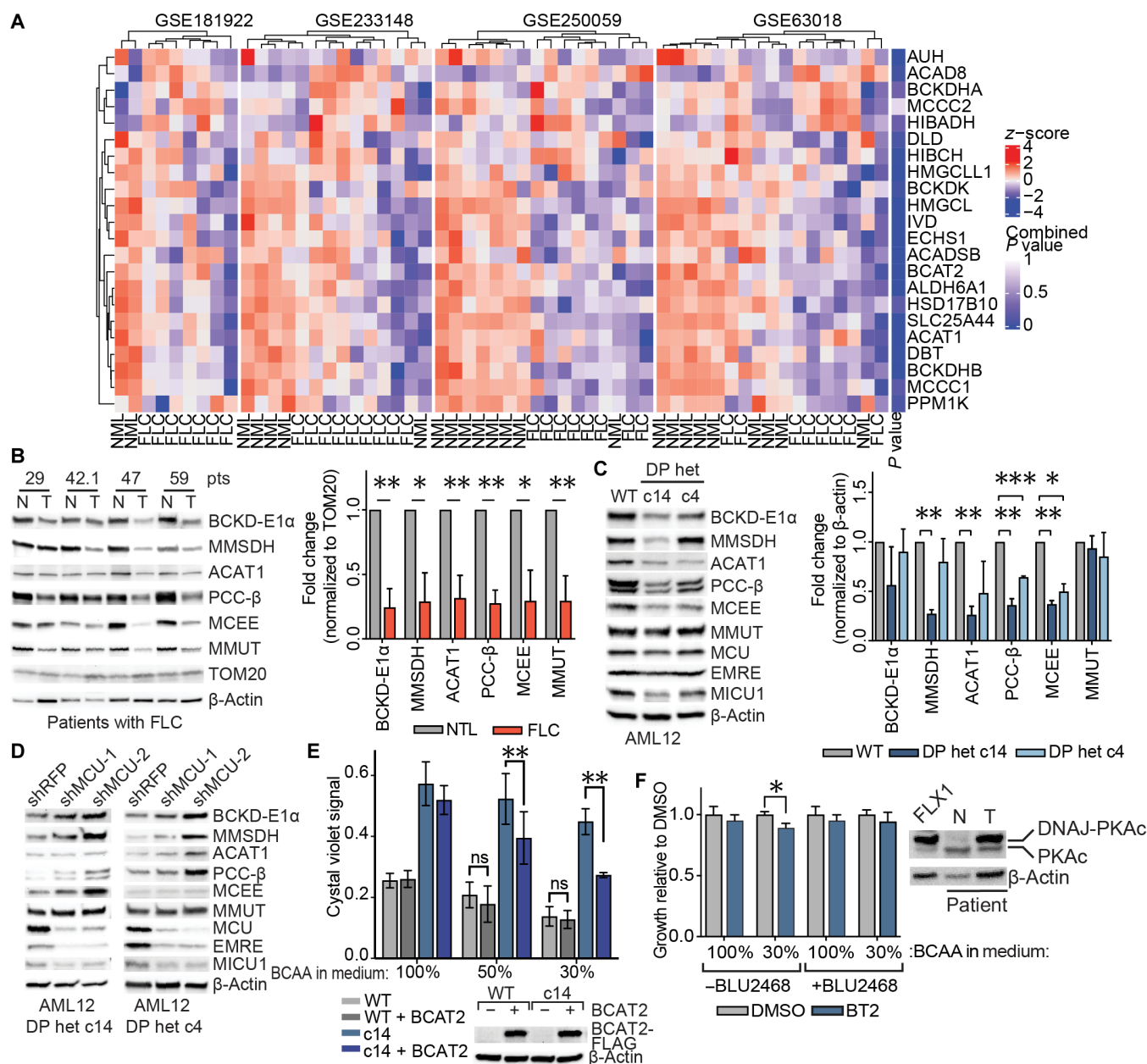
Fig. 6. FLC is characterized by uniporter-mediated suppression of BCAA catabolism. (**A**) Analysis of publicly available gene expression datasets of FLC tumor and normal liver show decreases in BCAA catabolism gene expression in FLC. (**B**) Immunoblots of select BCAA catabolism enzymes from paired non-tumor (N) and FLC tumor (T) lysates and pooled quantification of protein levels normalized to TOM20 levels; statistical significance was determined by one-sample *t* test. (**C**) Immunoblots and quantification of select BCAA catabolism proteins and uniporter components in AML12 cells; statistical significance was determined by one-sample *t* test; *n* = 4. (**D**) MCU KD increases expression of BCAA catabolism pathway proteins in FLC clones; immunoblots of select pathway proteins and uniporter components are shown. (**E**) Growth of AML12 cells with or without BCAT2 expression, grown in medium with varying BCAA levels; statistical significance was determined by two-way ANOVA, *n* = 2 (three technical replicates each). Immunoblot of BCAT2 confirms its expression. (**F**) Growth of FLX1 under indicated conditions; statistical significance was determined by Šídák's multiple comparisons test, *n* = 2. Immunoblot shows DP expression in FLX1 lysates and tumor (T) but not in non-tumor (N) liver lysates from a patient with FLC. All error bars indicate SD; *$P < 0.05$; **$P < 0.01$; ***$P < 0.001$. *n* indicates the number of biological replicates.

Ca^{2+} signaling remains to be investigated, we delineate a pathway that starts with DP-induced activation of mitochondrial Ca^{2+} signaling and subsequent KLF15-dependent transcriptional changes, urea cycle defects, and, possibly, fibrosis in FLC.

Our results indicate that the transcription factor KLF15, a known regulator of BCAA catabolism enzymes (*57*, *69*), mediates the effects of MCU on BCAA pathway gene expression. This suggests that KLF15 may play a broader role in transcriptional regulation of metabolism by mitochondrial Ca^{2+} signaling, especially in the context of cancer. Reduction in KLF15 levels has been correlated with tumor growth and poor prognosis in several types of cancer (*70*–*75*). However, KLF15 expression changes have not been implicated in liver cancer.
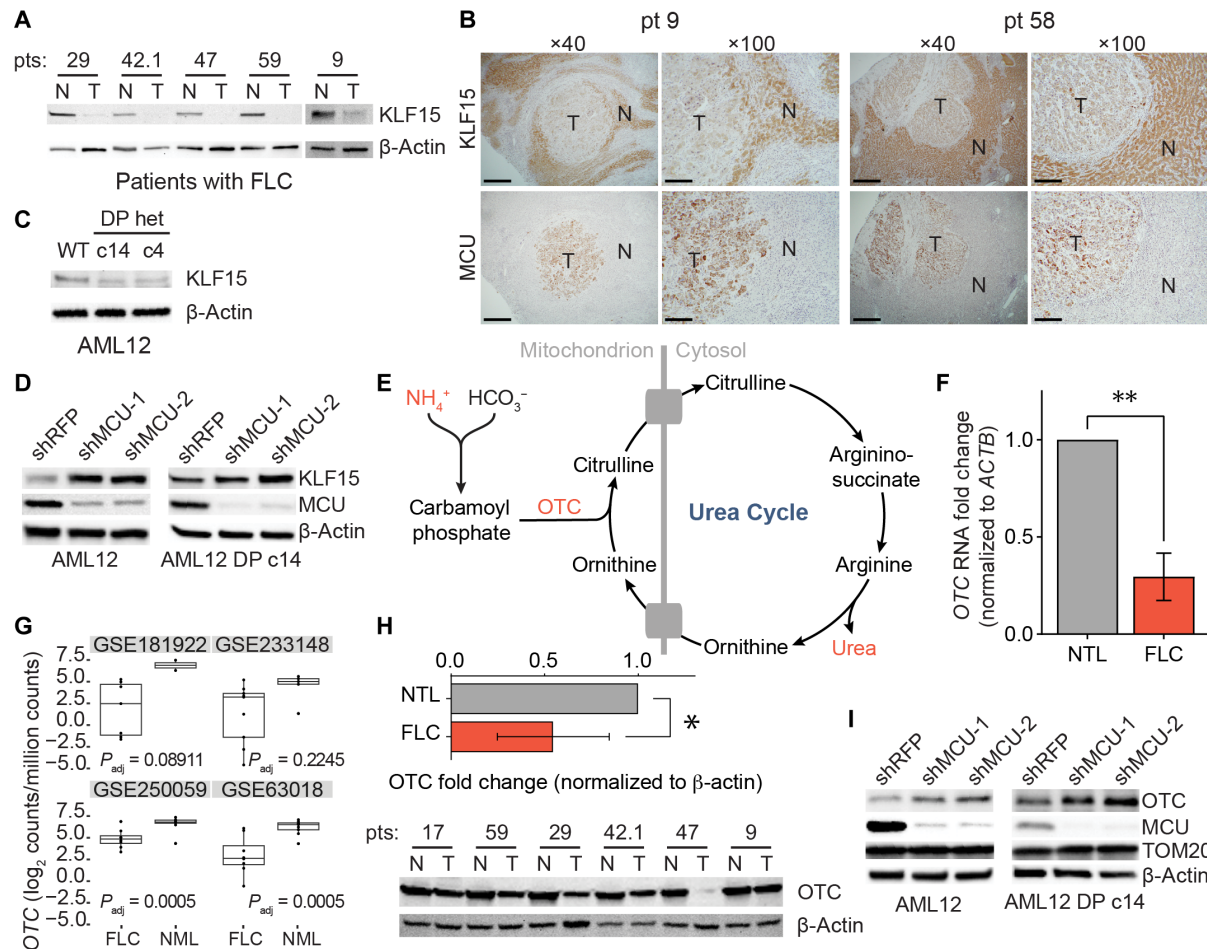
Fig. 7. KLF15 and OTC expression are regulated by the uniporter in FLC. (**A**) Immunoblots of KLF15 in paired non-tumor (N) and FLC tumor (T) lysates. (**B**) IHC of MCU and KLF15 on non-tumor (N) and tumor (T) regions from FLC patients 9 and 58; ×40 and ×100 image scale bars are 500 and 200 μm, respectively. (**C**) Immunoblot of KLF15 from WT AML12, c14, and c4 lysates. (**D**) Immunoblots of KLF15 from WT AML12 and c14 lysates following MCU KD. (**E**) Schematic of the urea cycle metabolites and OTC, a mitochondrial protein with reduced levels in FLC. (**F**) qPCR analysis of *OTC* mRNA expression in paired NTL and tumors from FLC patients 29, 42.1, 47, and 59; statistical significance was determined by one sample *t* test; $n = 4$ (**G**) *OTC* mRNA expression in normal liver (NML) and FLC tumors in the indicated gene expression datasets. (**H**) Immunoblot of OTC and quantification of OTC levels relative to β-actin from paired non-tumor (N) and FLC tumor (T) lysates; statistical significance was determined by one sample *t* test; $n = 5$. (**I**) Immunoblots of OTC from WT AML12 and c14 lysates following MCU KD. All error bars indicate SD; *$P < 0.05$; **$P < 0.01$. *n* indicates the number of biological replicates.

The MCU/KLF15/BCAA catabolism signaling axis that we identified in FLC may also play a role in other forms of cancer. On the basis of analysis of The Cancer Genome Atlas, the BCAA catabolism pathway is down-regulated in ~70% of cancers (*52*). Additionally, both suppressed BCAA catabolism and increased uniporter activity correlate with poor patient prognosis in hepatic cancers (*52*, *76–78*). This raises the intriguing possibility that uniporter-mediated metabolic changes may be a more general mechanism of metabolic regulation in cancer, whereby increased mitochondrial Ca^{2+} levels stimulate TCA cycle activity, down-regulate BCAA catabolism, and conserve essential amino acids for protein synthesis and cell proliferation.

Most BCAA catabolism occurs in skeletal muscle, adipose tissue, and the liver (*68*). The initial conversion of BCAAs to α-ketoacids is catalyzed by cytosolic BCAT1 and mitochondrial BCAT2 enzyme. Recent findings suggest that human and murine liver show differences in liver BCAT activity (*54*, *79*). BCAT activity is present in the

human liver, whereas murine hepatocytes, including the AML12 model that we used in this study, lack BCAT activity, limiting assessment of pathway activity in this model. To overcome this limitation and to recapitulate human hepatocyte BCAA metabolism, we expressed BCAT2 in AML12 cells. This enabled us to investigate the importance of this pathway in FLC growth, especially when cells were grown in medium with more physiological BCAA concentrations (30% BCAA medium). Growth impairment in FLC cellular models after activation of BCAA catabolism underscores the importance of the DP-MCU axis in FLC pathogenesis. Whether additional FLC-specific metabolic adaptations are regulated by mitochondrial calcium signaling remains to be seen.

PKA signaling regulates many aspects of cancer biology (*80*). Our work presents a mitochondrial Ca^{2+} signaling-dependent mechanism downstream of PKA signaling that regulates cancer metabolism. Although the means by which DP expression increases MCU activity remains to be identified, our work suggests that MCU and
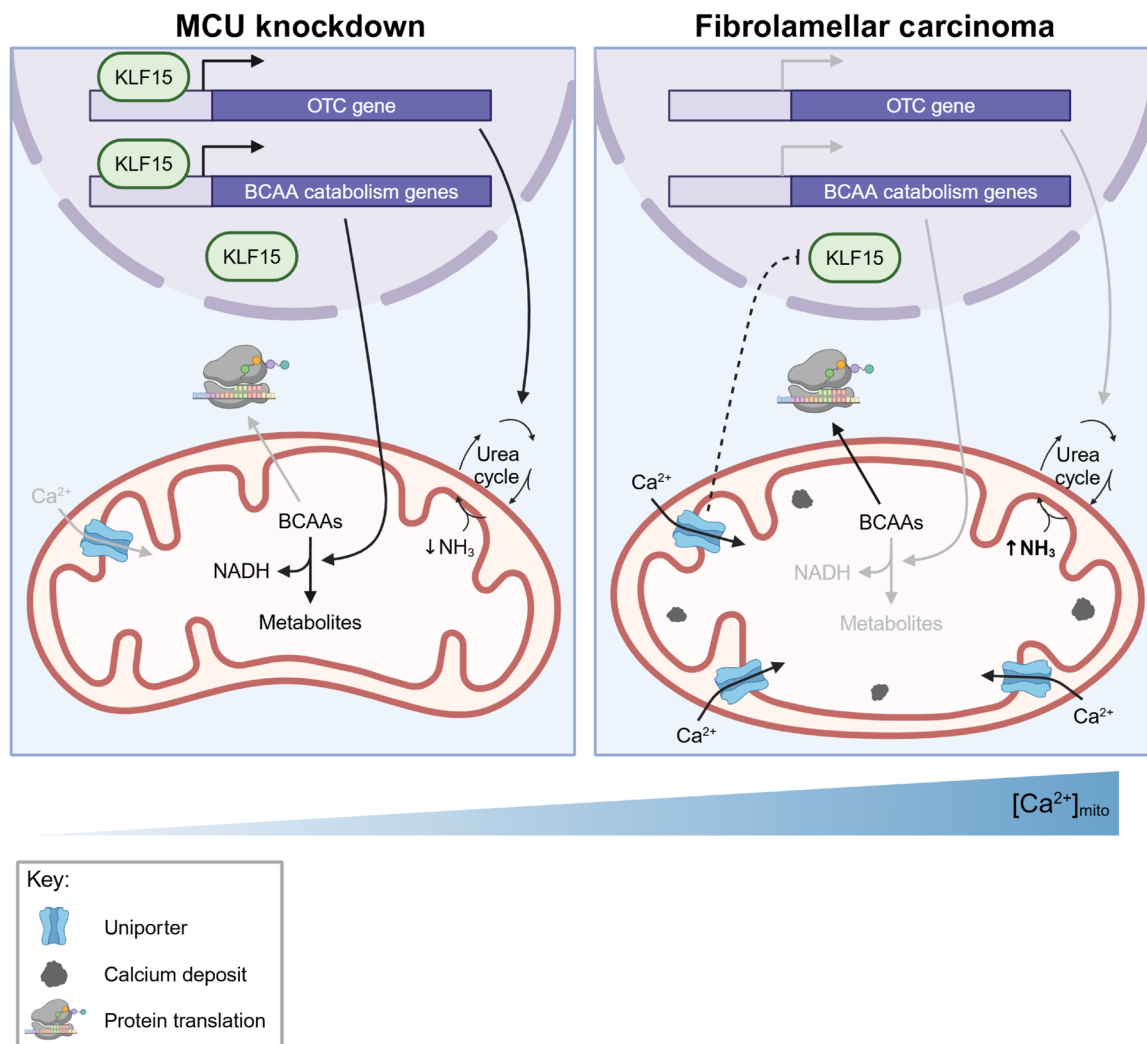
Fig. 8. Model for regulation of KLF15, BCAAs, and the urea cycle by mitochondrial Ca^{2+} signaling. Our data suggest that, under conditions of low uniporter function, high KLF15 levels stimulate expression of BCAA catabolism pathway genes and OTC. Activation of this pathway helps maintain NADH/NAD$^+$ balance. Increased uniporter activity, as observed in FLC, inhibits KLF15, leading to decreased BCAA catabolism enzyme and OTC expression. This inhibition conserves BCAAs for translation and cell growth. MCU inhibition also causes urea cycle impairment, which can lead to hyperammonemia. How the uniporter regulates KLF15 expression is not known. This diagram was created in BioRender (N. Marsh, 2025; https://BioRender.com/akf16h3).

KLF15 are potential therapeutic targets in the treatment of FLC and its sequelae.

MATERIALS AND METHODS
Cell lines and tissue culture
All cell lines were grown in a standard tissue culture incubator (VWR, 75875-212) at 37°C with 5% CO_2. HeLa cells were cultured in Dulbecco's modified Eagle medium (DMEM; Thermo Fisher Scientific, 11-965-118) supplemented with 10% fetal bovine serum (FBS) (VWR, 89510-186), 2 mM GlutaMAX (Thermo Fisher Scientific, 35-050-061), and penicillin (100 IU/ml) and streptomycin (100 μg/ml; VWR, 45000-652). HeLa cells were obtained from the Whitehead Institute for Biomedical Research. The HeLa cell line has the following short tandem repeat profile: D5S818 (11, 12), D13S317 (12, 13.3),

D7S820 (8, 12), D16S539 (9, 10), vWA (16, 18), TH01 (7), AMEL (X), TPOX (8, 12), and CSF1PO (9, 10). This profile is a 94% match to HeLa cervical adenocarcinoma (human) [CCL-2; American Type Culture Collection (ATCC)] according to the analysis performed by the ATCC database. AML12 cells were cultured in DMEM/F-12 medium (Gibco, 11330057) supplemented with 10% FBS (VWR, 89510-186), 1× insulin-transferrin-selenium (Gibco, 41400045), dexamethasone (40 ng/ml; MP Biomedicals, 0219456180), and penicillin (100 IU/ml) and streptomycin (100 μg/ml; VWR, 45000-652). AML12 cells were obtained from ATCC (CRL-2254, lot no. 70039497), and CRISPR-edited AML12 DP clones c14 and c4 were generated and validated by the Scott Lab as described (45). All cell lines were tested for mycoplasma using the Genlantis MycoScope PCR Detection Kit (VWR, 10497-508) and were confirmed to be free of mycoplasma contamination. FLAG-BCAT2 construct was obtained from Addgene (196204).

Generation of KO and rescue cell lines

Broad Institute guide RNA (gRNA) sequences for *MCU* (TGAACT-GACACAGCGTTCACGC) and *EMRE* (GTCTCAGCCAGGTACC-GTCG) were each cloned into the pU6T7 vector (Addgene, 71462). Five million HeLa cells were resuspended in 400 µl of DMEM with 2 µg of SpCas9 plasmid (Addgene, 71814), 500 ng of gRNA plasmid, and 17.5 µg of pUC19 plasmid (Addgene, 50005). The cells and DNA were transferred to a cuvette, incubated on ice for 5 min, and electroporated at 200 V with a capacitance of 950 µF and pulse length of 23 ms. Electroporated cells were allowed to grow to confluence on a 10-cm plate before being diluted to one cell/200 µl and plated in 96-well plates to obtain single-cell clones. HeLa MCU KO and EMRE KO clones were verified by Western blotting, functional assays, and sequencing. To rescue MCU expression, MCU KO clone 18 was infected with lentivirus containing an MCU-FLAG construct with the sequence below. Following resistance marker selection, single-cell clones were isolated and screened for MCU expression by Western blot.

MCU-FLAG DNA sequence

ATGGCGGCCGCCGCAGGTAGATCGCTCCTGCTGCTCCTCTCC-
TCTCGGGGCGGCGGCGGCGGGGGCGCCGGCGGCTGCGGGGC-
GCTGACTGCCGGCTGCTTCCCTGGGCTGGGCGTCAGCCGCCAC-
CGGCAGCAGCAGCACCACCGGACGGTACACCAGAGGATC-
GCTTCCTGGCAGAATTTGGGAGCTGTTTATTGCAGCACTGTTGT-
GCCCTCTGATGATGTTACAGTGGTTTATCAAAATGGGTTACCT-
GTGATATCTGTGAGGCTACCATCCCGGCGTGAACGCTGT-
CAGTTCACACTCAAGCCTATCTCTGACTCTGTTGGTGTATTTT-
TACGACAACTGCAAGAAGAGGATCGGGGAATTGACAGAGTTGC-
TATCTATTCACCAGATGGTGTTCGCGTTGCTGCTTCAACAG-
GAATAGACCTCCTCCTCCTTGATGACTTTAAGCTGGTCATTAAT-
GACTTAACATACCACGTACGACCACCAAAAAGAGACCTCTTA-
AGTCATGAAAATGCAGCAACGCTGAATGATGTAAAGACATTG-
GTCCAGCAACTATACACCACACTGTGCATTGAGCAGCACCAGT-
TAAACAAGGAAAGGGAGCTTATTGAAAGACTAGAGGATCT-
CAAAGAGCAGCTGGCTCCCCTGGAAAAGGTACGAATTGAGA-
TTAGCAGAAAAGCTGAGAAGAGGACCACTTTGGTGC-
TATGGGGTGGCCTTGCCTACATGGCCACACAGTTTGGCATTTTG-
GCCCGGCTTACCTGGTGGGAATATTCCTGGGACATCATGGAGC-
CAGTAACATACTTCATCACTTATGGAAGTGCCATGGCAATGTATG-
CATATTTTGTAATGACACGCCAGGAATATGTTTATCCAGAAGC-
CAGAGACAGACAATACTTACTATTTTTCCATAAAGGAGC-
CAAAAAGTCACGTTTTGACCTAGAGAAATACAATCAACT-
CAAGGATGCAATTGCTCAGGCAGAAATGGACCTTAAGAGACT-
GAGAGACCCATTACAAGTACATCTGCCTCTCCGACAAATTGGT-
GAAAAAGATTCTAGAGGTGGATCTGGTGGATCTGGTGGATC-
TATGGATTACAAGGATGACGATGACAAG.

Proliferation assays

A total of 20,000 HeLa cells were plated in six-well plates on day 0. On days 2, 3, and 5, the medium was aspirated, and the cells were washed with phosphate-buffered saline (PBS; Thermo Fisher Scientific, 20012050), detached with 200 µl of trypsin solution (Gibco, 12605-010), and then resuspended in 1.8 ml of medium for a total volume of 2 ml. The resuspended cells were counted using a Beckman Coulter Z2 Cell and Particle Counter (Beckman Coulter, 383550). A total of 100,000 AML12 cells were plated in 10-cm plates on day 0. On days 2, 3, and 4, the medium was aspirated, and the cells were washed with PBS (Thermo Fisher Scientific, 20012050), detached with 2 ml of trypsin solution (Gibco, 12605-010), and then resuspended in 4 ml of medium, for a total volume of 6 ml. The resuspended cells were counted using a Coulter Z2 Cell and Particle Counter (Beckman Coulter, 383550).

MS sample preparation

Five replicates of 500,000 WT and MCU KO HeLa cells were plated in 10-cm plates. After 48 hours, the medium was aspirated, and cells were washed with cold PBS (Thermo Fisher Scientific, 20012050) and lysed with 350 µl of fresh lysis buffer consisting of 8 M urea (Sigma-Aldrich, U5128), 1 M tris, 1 M tris(2-carboxyethyl)phosphine hydrochloride (Sigma-Aldrich, C4706), and 0.6 M 2-chloroacetamide (Sigma-Aldrich, C0267). Lysates were sonicated on ice for 10 min with 30-s on/off pulses at an amplitude setting of 100 in a cup-horn sonicator. Samples were vortexed at 1400 rpm on a ThermoMixer (Eppendorf) for 30 min at 37°C. Samples were then centrifuged at 17,000*g* for 10 min at 4°C, and 175 µl of the supernatant was transferred to a new tube. Cold acetone (700 µl) was added to each sample. Trichloroacetic acid (43.75 µl; Sigma-Aldrich, T4885) was then added for a final concentration of 5%. The samples were vortexed briefly at 1400 rpm and stored overnight at −20°C. Samples were centrifuged at 6000*g* for 10 min at 4°C, and the supernatant was aspirated. Cold acetone (500 µl) was added to the pellet, and the pellet was sonicated in an ice bath until the pellet was dissolved (5 to 10 min). The samples were incubated on ice for another 15 min and then centrifuged at 6000*g* for 10 min at 4°C. The supernatant was aspirated, and the pellets were air dried for 2 to 3 min. Samples were resuspended in 200 µl of 8 M urea and 100 mM tris solution. Samples were vortexed for 1 hour at 37°C to dissolve the pellet in solution. Protein concentrations were measured with the Pierce 660-nm Protein Assay (Thermo Fisher Scientific, 22660), and 500 µg of protein per sample was used for subsequent mass spectrometry (MS) experiments. Samples were diluted 1:1 with 100 mM triethylammonium bicarbonate (TEAB; Sigma-Aldrich, T7408), reducing the urea concentration to 4 M. A stock of Lys-C endoproteinase (2 µg/µl; Fujifilm Wako Chemicals, 121-05063) was added to each sample for an enzyme:protein ratio of 1:100. Samples were vortexed at 1400 rpm for 2 hours at 37°C. Samples were again diluted 1:1 with 100 mM TEAB, bringing the urea concentration to 2 M. Stock of trypsin (0.5 µg/µl; Promega, V5111) dissolved in 40 mM acetic acid was added to each sample for an enzyme:protein ratio of 1:100. Samples were vortexed at 1400 rpm overnight at 37°C. The following day, high-performance liquid chromatography (HPLC)–grade formic acid (Sigma-Aldrich, 5438040100) was added for a final concentration of 2% (v/v). Samples were centrifuged at 11,000*g* for 5 min. Five percent of the supernatant was used for stage tipping. C_{18} StageTips were made as described by Rappsilber *et al.* (*81*). StageTips were washed with sequential washes of 50 µl of HPLC-grade methanol (Sigma-Aldrich, 494291), Buffer B, and Buffer A, centrifuging the tips at 1800*g* for 2 min between each wash. Buffer B consisted of 0.1% HPLC-grade trifluoroacetic acid (TFA; Alfa Aesar, AA446305Y) and 80% HPLC-grade acetonitrile (Sigma-Aldrich, 271004). Buffer A consisted of 0.1% TFA and 5% acetonitrile. Samples were loaded on the StageTips, centrifuged at 1800*g* for 2 min, and washed again with Buffer A.

LC-MS/MS–based proteomics and data analysis

Peptide samples were separated on an EASY-nLC 1200 System (Thermo Fisher Scientific) using 20-cm-long fused silica capillary

columns (100-μm inside diameter, laser pulled in-house with Sutter P-2000, Novato CA) packed with 3-μm 120-Å reversed-phase C18 beads (Dr. Maisch, Ammerbuch, DE). The liquid chromatography (LC) gradient was 90 min long with 5 to 35% B at 300 nl/min. LC solvent A was 0.1% (v/v) aqueous acetic acid, and LC solvent B was 20% 0.1% (v/v) acetic acid and 80% acetonitrile. MS data were collected with a Thermo Fisher Scientific Orbitrap Fusion Lumos. The MS method used was a data-independent acquisition (DIA) method with a 120K resolution MS1 scan from mass/charge ratio (m/z) 395 to 1005 and 15K resolution MS2 scans with 12 Thomson (Th) isolation with m/z between 400 and 1000; the AGC target was 400,000 ions with a maximum injection time of 25 ms. Raw files were analyzed with MSFragger 3.4 (82) and DIA-nn 1.8 (83) using protein and peptide false discovery rates of 0.01. The FASTA database used for search was a human Uniprot reference database downloaded 2021-11-08, with "stricttrypsin" and two missed cleavages permitted. Variable modifications were N-term acetylation, pyroGlu-, and loss of ammonia (−17.0265 nQnC) at peptide N termini. Carbamidomethyl (C) was a fixed modification. Data were further processed using the Perseus software package (version 1.5.2.6), the R environment, Origin Pro 8.0, and Microsoft Excel. Gene Ontology (GO) term enrichment analysis was performed using the ShinyGO 0.76 web application (http://bioinformatics.sdstate.edu/go/) (36). LC–tandem MS (LC-MS/MS) data accession numbers are as follows: MassIVE, MSV000096493; and ProteomeXchange, PXD058152.

RNA sequencing

A total of 500,000 HeLa cells were plated in six-well plates. After 2 days, total RNA was isolated using an RNeasy kit (QIAGEN, 74106). Samples were sent to Genewiz for sequencing and data analysis, as follows: Samples underwent mRNA enrichment, mRNA fragmentation, and random priming. Genewiz performed first- and second-strand cDNA synthesis followed by end repair, 5′ phosphorylation, and dA-tailing. cDNA was sequenced, following adaptor ligation and enrichment by PCR. During analysis, the reads were trimmed and mapped to the *Homo sapiens* GRCh38 reference genome available (84) (www.ensembl.org) using the STAR aligner (v.2.5.2b). Hit counts for genes and exons were calculated with featureCounts (Subread package, v.1.5.2). DESeq2 was used for analysis of differential gene expression. P values and $\log_2$ fold changes were determined with the Wald test, and genes with an adjusted P value < 0.05 and absolute $\log_2$ fold change > 1 were considered to be differentially expressed.

Seahorse metabolic flux analysis

HeLa and AML12 cells were seeded at 10,000 or 15,000 cells per well, respectively, in a XFe96 Microplate (Agilent Technologies, 103792-100) and cultured overnight at 37°C in 5% CO_2. The Extracellular Flux Assay Kit oxygen probes (Agilent Technologies, 103792-100) were activated in XF calibrant buffer (Agilent, 100840-000) at 37°C in a non-CO_2 incubator overnight. Seahorse XF medium was prepared fresh by supplementing XF DMEM (pH 7.4; Agilent, 103575-100) with 100 mM pyruvate solution (Agilent, 103578-100), 1 M glucose solution (Agilent, 103577-100), and 200 mM L-glutamine (Thermo Fisher Scientific, BP379-100). The cell culture medium was removed from the plate, and the cells were washed once with pre-warmed Seahorse XF medium and replaced with fresh medium a second time. The cells were then incubated in a CO_2-free incubator at 37°C for 1 hour. OCR measurements were performed with a Seahorse XFe96 Extracellular Flux Analyzer (Agilent, S7800B) using the Cell Mito Stress Test program. The sensor cartridge was loaded with drugs and inserted into the machine 30 min before the flux assay to calibrate the oxygen probes. Following measurements of baseline cellular respiration, respiration was measured after addition of oligomycin, carbonyl cyanide p-trifluoromethoxyphenylhydrazone (FCCP), and antimycin A and rotenone together, with final concentrations of 1 μM. OCR was analyzed with the Seahorse XF Cell Mito Stress Test Report Generator (Wave Software). OCR measurements were normalized to cell number as determined by the CyQUANT Cell Proliferation Assay Kit (Thermo Fisher Scientific, C7026) or 4′,6-diamidino-2-phenylindole (DAPI) staining for HeLa and AML12 cells, respectively. For the CyQUANT assay, the medium was removed from each well and the plates were frozen at −80°C for >1 hour to lyse the cells. CyQUANT was used per the manufacturer's instructions to measure fluorescence intensity [excitation (Ex), 480 nm; and emission (Em), 520 nm]. For DAPI staining, 40 μl of medium was left in each well, and cells were frozen at −80°C for >1 hour to lyse the cells. After thawing, 100 μl of DAPI (1 μg/μl; Thermo Fisher Scientific, 62248) was added to each well for 5 min before measuring DAPI fluorescence (Ex, 359 nm; and Em, 457 nm).

LC-MS–based lipid analysis

Cell pellets containing 10 million HeLa cells per condition were frozen at −80°C until lipid extraction. Lipid extraction and analysis were carried out as described (85). Briefly, cell pellets were resuspended in methanol and sonicated three times for 30 s while on ice. The homogenized solution was centrifuged at 16,900g for 15 min at 4°C. Supernatant (800 μl) was removed into a fresh 4-dram vial. Cold methanol (1 ml) was added to the remaining pellet, sonicated, and centrifuged again. This supernatant was combined with the previous extract and dried down using a nitrogen evaporator. LC-MS data were acquired using an Agilent 1260 HPLC with an Agilent 6530 Quadrupole Time-of-Flight mass spectrometer. A Luna C5 reverse-phase column (5 m, 4.6 mm by 50 mm, Phenomenex) was used for positive mode and a Gemini C18 reversed-phase column (5 m, 4.6 mm by 50 mm, Phenomenex) was used in negative mode. Mobile phase A was 95:5 water:methanol, and mobile phase B was 60:35:5 isopropanol:methanol:water for both negative and positive modes. The mobile phases contained additives to aid electrospray ionization and improve ion detection (0.1% formic acid in positive mode; 5 mM ammonium formate and 0.1% ammonium hydroxide in negative mode). Data acquisition in positive and negative mode used different gradients: Ramping from 0% mobile phase B to 100% mobile phase B occurred over 45 and 65 min for positive and negative mode, respectively. For both methods, the flow rate was set to 0.1 ml/min for the first 5 min at 100% mobile phase A and then increased to 0.5 ml/min for the remainder of the run. A dual electrospray ionization source was used; capillary and fragmentor voltages were set to 3500 and 175 V, respectively. All data were collected in the extended dynamic range mode (m/z = 50 to 1700). Representative lipid species for each class were targeted by extracting the corresponding m/z for each ion in MassHunter Qualitative Analysis software (version B.06.00, Agilent Technologies). Peak areas were manually integrated and represented as abundance. Relative abundance values were calculated by dividing the abundance of a lipid by the average abundance of that lipid in the WT set.

Cell lysate preparation and immunoblots

Cells were grown to 40 to 80% confluency, and, then, plates were washed with cold PBS (Thermo Fisher Scientific, 20012050) on ice

and lysed with either radioimmunoprecipitation assay (RIPA) or triton lysis buffer. RIPA buffer consisted of 50 mM Hepes-KOH (pH 7.4; Sigma-Aldrich, H3375; MilliporeSigma, 1050121000), 150 mM NaCl (Sigma-Aldrich, 746398), 2 mM EDTA (Sigma-Aldrich, 607-429-00-8), 10 mM sodium pyrophosphate (Sigma-Aldrich, 71501), 10 mM β-glycerophosphate (Sigma-Aldrich, G9422), 1% sodium deoxycholate (Sigma-Aldrich, D6750), 0.1% SDS (Sigma-Aldrich, L4509), and 1% Triton X-100 (Sigma-Aldrich, X100). Triton buffer consisted of 50 mM Hepes-KOH (pH 7.4), 40 mM NaCl, 2 mM EDTA, 10 mM β-glycerophosphate, 1.5 mM sodium orthovanadate (Sigma-Aldrich, S6508), 50 mM sodium fluoride (Sigma-Aldrich, S7920), 10 mM sodium pyrophosphate, and 1% Triton X-100. Lysis buffers were supplemented with protease inhibitors (Sigma-Aldrich, 11836170001) immediately before lysis. Lysates were centrifuged at 17,000g for 10 min at 4°C. The supernatants were normalized by protein concentration as measured by either a Bradford protein assay (Bio-Rad, 5000205) or Pierce BCA assay (Thermo Fisher Scientific, 23209) and a BioTek Synergy H1 plate reader (Thermo Fisher Scientific, 11-120-536). SDS–polyacrylamide gel electrophoresis (PAGE) samples were prepared from the lysates with 5× reducing sample buffer (pH 6.8) consisting of 10% SDS, 25% 2-mercaptoethanol (Sigma-Aldrich, M3148), 25% glycerol (Sigma-Aldrich, G5516), 50 mM tris-HCl (Sigma-Aldrich, RDD008), and 0.1% bromophenol blue (VWR, 97061-690).

Samples were heated to 95°C for 5 min and then brought to room temperature. Samples were mixed by pipetting and loaded onto 4 to 15% gradient Mini-PROTEAN TGX gels (Bio-Rad, 4561086). Following gel electrophoresis in tris-glycine-SDS running buffer (Boston BioProducts, BP-150), proteins were transferred to ethanol-activated 0.2-μm polyvinylidene difluoride membranes (Bio-Rad, 1620174) using the BioRad Mixed Molecular Weight Protein Transfer setting (7 min, 1.3 A, 25 V) on the Trans-Blot Turbo Transfer System (Bio-Rad, 1704150) with Trans-Blot Turbo Transfer Buffer (Bio-Rad, 10026938). After transfer, membranes were washed in 20% ethanol for ~2 min and checked for equal loading and even transfer by Ponceau stain (Sigma-Aldrich, P7170). Membranes were then incubated with 1% w/v bovine serum albumin (BSA; Sigma-Aldrich, A2153) in tris-buffered saline (TBS) with 1% (v/v) Tween 20 (Boston Bio-Products, IBB-180) at room temperature for 1 to 4 hours. Membranes were incubated overnight with primary antibody and 1% BSA in TBST at 4°C. All membranes were then washed with TBST three times, 5 min each, and incubated with secondary antibody and 1% BSA in TBST for 1 hour using a BlotCycler W5 (Precision Biosystems). Membranes were washed four times, 5 min each, with TBST. Membranes were developed using Clarity Western ECL substrate (Bio-Rad, 170-5060) or Clarity Max Western ECL substrate (Bio-Rad, 1705062). Immunoblots were imaged with an iBrightCL1000 imager (Life Technologies, A23749) and quantified using the Image Studio Lite software, version 5.2 (LI-COR Biosciences). The following antibodies and dilutions were used: 1:3000 rabbit ACAT1 antibody (ABclonal, A13273); 1:3000 rabbit BCKDHA antibody (ABclonal, A21588); 1:5000 mouse β-actin antibody (Cell Signaling Technology, 3700); 1:5000 rabbit EMRE antibody (Bethyl Laboratories, A300-BL19208); 1:3000 rabbit HSP60 antibody (Cell Signaling Technology, 12165); 1:3000 rabbit KLF15 antibody (ABclonal, A7194); 1:3000 rabbit MCEE antibody (ABclonal, A14430); 1:3000 rabbit MCU antibody (Cell Signaling Technology, 14997); 1:3000 rabbit MICU1 antibody (ABclonal, A21948); 1:3000 rabbit MMSDH antibody (ABclonal, A3309); 1:3000 rabbit MMUT antibody (ABclonal, A3969); 1:1000

mouse OTC antibody (Invitrogen, PAS-28197); 1:3000 rabbit PCCB antibody (ABclonal, A5415); 1:3000 rabbit phospho-BCKDH-E1α and human S292/mouse S293 antibody (Cell Signaling Technology, 40368); 1:1000 rabbit phospho-R-X-S*/T* (Cell Signaling Technology, 9621); 1:3000 rabbit PKA-Cα antibody (BD Biosciences, 610980); 1:3000 rabbit TOM20 antibody (Cell Signaling Technology, 42406); 1:3000 rabbit BCKDK antibody (ABclonal, A20909); 1:10,000 HRP-linked α-rabbit secondary antibody (Cell Signaling Technology, 7074); and 1:10,000 HRP-linked α-mouse secondary antibody (Cell Signaling Technology, 7076).

Isolation of patient samples
Fresh NTL and FLC tumor samples were procured from patients undergoing liver resection for FLC treatment. Before surgery, written informed consent was obtained for tissue donation under a research protocol approved by the University of Washington Institutional Review Board (IRB) (no. 1852) and Seattle Children's Hospital IRB (no. 15277). All research samples were de-identified. Clinical details for each patient are outlined in table S1. NTL and FLC samples were processed and transferred to the laboratory on ice within 1 hour of tissue excision. Samples were stored at −80°C before lysate preparation.

Lysis and sample preparation of patient samples
Tissues were lysed with protease inhibitor-supplemented RIPA buffer using a TissueRuptor homogenizer (QIAGEN, 9002755). Tissues were homogenized until they were a uniform consistency. Samples were then centrifuged at 17,000g for 10 min at 4°C and prepared for SDS-PAGE with 5× reducing sample buffer.

Generation of shRNA constructs
shRNA sequences were designed by the RNAi Consortium (TRC) of the Broad Institute. Forward and reverse oligos encoding the shRNA were annealed to form dsDNA. Forward oligo (100 pmol) and reverse oligo (100 pmol) were resuspended in 25 μl of 1× NEBuffer 2 [New England Biolabs (NEB), B7002S]. The solution was incubated in a 95°C water bath for 4 min and then slowly cooled (~0.5°C/min) to room temperature. The pLKO.1 vector (Addgene, 10878) was digested with Age I–HF (NEB, R3552) and Eco RI–HF (NEB, R3101) and ligated with the oligo solution according to the NEB Quick Ligase (NEB, M2200) protocol. The ligation mixture was transformed into XL10-Gold competent cells (Agilent, 200315). Resulting plasmids were verified by sequencing.

Mouse shMCU-1, forward oligo: CCGGGATCCGAGATGACC-GTGAATCCTCGAGGATTCACGGTCATCTCGGATCTTTTTG; reverse oligo: AATTCAAAAAGATCCGAGATGACCGTGAATCCT-CGAGGATTCACGGTCATCTCGGATC. Mouse shMCU-2, forward oligo: CCGGTAGGGAATAAAGGGATCTTAACTCGAGTTAAGATC-CCTTTATTCCCTATTTTTG; reverse oligo: AATTCAAAAAT-AGGGAATAAAGGGATCTTAACTCGAGTTAAGATC-CCTTTATTCCCTA. shGFP control, forward oligo: CCGGCCAC ATGAAGCAGCACGACTTCTCGAGAAGTCGTGCTGCT-TCATGTGGTTTTTG; reverse oligo: AATTCAAAAACCACATGA-AGCAGCACGACTTCTCGAGAAGTCGTGCTGCTTCATGT GG. shRFP control, forward oligo: CCGGGCTCCGTGAACGGC-CACGAGTCTCGAGACTCGTGGCCGTTCACGGAGCTTTTTG; reverse oligo: AATTCAAAAAGCTCCGTGAACGGCCACGAG-TCTCGAGACTCGTGGCCGTTCACGGAGC. Human shBCKDK-1, forward oligo: CCGGGACAGACTTCCCTCCGATCAACTCGAGTT-GATCGGAGGGAAGTCTGTCTTTTTG; reverse oligo: AATTCAAA

AAGACAGACTTCCCTCCGATCAACTCGAGTTGATCGG-AGGGAAGTCTGTC. Human shBCKDK-1, forward oligo: CCG-GCCCTACAATGTCCCAGATGTGCTCGAGCACATCTGGGA-CATTGTAGGGTTTTTG; reverse oligo: AATTCAAAAACCCT ACAATGTCCCAGATGTGCTCGAGCACATCTGGGACA-TTGTAGGG.

Lentivirus production and transduction
One million human embryonic kidney (HEK) 293T cells (from the Whitehead Institute for Biomedical Research) were plated in 6-cm plates. The following day, cells were transfected. 100 ng of p-CMV-VSV-G (Addgene, 8454), 900 ng of psPax2 (Addgene, 12260), and 1 μg of viral plasmid were diluted in 6 μl of X-tremeGENE 9 DNA transfection reagent (Sigma-Aldrich, 6365787001) and 150 μl of DMEM and incubated at room temperature for 15 min before being added to the cells. After 36 to 48 hours, the virus-containing medium was filtered through a 0.45-μm sterile filter (VWR, 28145-505) and stored at −20°C until use. A total of 200,000 HeLa or 100,000 AML12 cells were plated in six-well plates. The following day, 200 μl of the virus-containing medium and polybrene (8 μg/ml; Sigma-Aldrich, H9268) were added to the cells. Infected cells were selected for 48 hours with puromycin (2 μg/ml). For assays measuring transcriptional changes in the BCAA catabolism pathway, shMCU-infected cells were cultured for 2 to 3 weeks before harvesting.

RNA isolation, cDNA synthesis, and qPCR
AML12 cells were grown in six-well plates to ~80% confluency in triplicate. Tumor and NTL samples were stored in RNALater solution at −80°C before RNA extraction. RNA was isolated with the RNeasy Kit (QIAGEN, 74106). For liver samples, ~30 mg of tissue was homogenized using a TissueRuptor homogenizer (QIAGEN, 9002755) according to the kit protocol. RNA (100 ng) was used for cDNA synthesis using the Maxima First Strand cDNA synthesis kit (Thermo Fisher Scientific, K1641) according to the kit instructions. The resulting cDNA was diluted 1:30 in dH$_2$O, and either 1 or 2 μl of diluted cDNA was used for qPCR using Applied Biosystems Taq-Man Fast Advanced Master Mix (Thermo Fisher Scientific, 44-445-57) in a 384-well plate (Thermo Fisher Scientific, 43-098-49) using a QuantStudio 5 RT-PCR System (Thermo Fisher Scientific). The following Taqman probes were used: human *ACTB* (Thermo Fisher Scientific, 4331182-Hs01060665_g1), human *MCU* (Thermo Fisher Scientific, 4331182-Hs00293548_m1), and human *OTC* (Thermo Fisher Scientific, 4331182-Hs00166892_m1).

Immunohistochemistry
Fresh human FLC tissue from liver resections were fixed in formalin and paraffin-embedded. Sections (4 μm thick) were cut and placed on glass slides. Slides were stained with hematoxylin and eosin (H&E) using a H&E staining kit (Vector Laboratories, H-3502) according to supplied protocol. For IHC staining, slides were deparaffinized, rehydrated, and washed with TBST. After antigen retrieval in 10 mM sodium citrate (pH 6) and quenching of endogenous peroxidase activity with 3% H$_2$O$_2$, samples were blocked with 2.5% normal horse serum (NHS) before incubation with primary antibodies overnight at 4°C. The following primary antibodies were used: 1:300 KLF15 rabbit antibody (ABclonal, A7194) and 1:250 MCU rabbit antibody (Cell Signaling Technologies, 14997). Negative controls were treated with 2.5% NHS without primary antibodies. Signals were processed using the ImmPRESS HRP Horse Anti-Mouse (Vector Laboratories, MP-7402) and Anti-Rabbit (Vector Laboratories, MP-7401) Peroxidase Kits and ImmPACT DAB Substrate Kit Peroxidase (Vector Laboratories, SK-4105) according to the manufacturer's protocol. Slides were counterstained with hematoxylin QS, dehydrated, and mounted with VectaMount Express Mounting Medium.

Ca^{2+} uptake in permeabilized cells
Protocol is adapted from Sancak *et al.* (*10*). Cell medium was changed 1 to 2 hours before harvesting. Cells were detached with trypsin (Gibco, 12605-010) and resuspended in cell medium. One million HeLa cells or 0.5 million AML12 cells were centrifuged at 800*g* for 3 min. Cell pellets were washed with PBS (Thermo Fisher Scientific, 20012050), centrifuged at 800*g* for 3 min, and resuspended in 150 μl of KCl buffer. KCl buffer consists of 125 mM KCl (Sigma-Aldrich, 793590), 2 mM K$_2$HPO$_4$ (Sigma-Aldrich, P3786), 1 mM MgCl$_2$, (Sigma-Aldrich, M8266), and 20 mM Hepes (pH 7.2; Sigma-Aldrich, H3375) supplemented fresh with 5 mM glutamate (Sigma-Aldrich, G1251), 5 mM malate (Sigma-Aldrich, M7397), and 1 μM Oregon Green 488 Bapta-6F (Invitrogen, O23990). Digitonin (0.01 or 0.005%; Thermo Fisher Scientific, BN2006) was added for HeLa and AML12 cell assays, respectively. Cells were transferred to a black 96-well plate (Greiner Bio-One, 655076). Fluorescence (Ex, 485/20 nm; and Em, 520/20 nm) was monitored every 2 s for 136 s at room temperature using a BioTek Synergy H1 microplate reader (Thermo Fisher Scientific, 11-120-536) before and after injection of 50 μM CaCl$_2$ (Sigma-Aldrich, 746495). Ca^{2+} uptake rates were calculated using the linear fit of uptake data points between 20 and 30 s after Ca^{2+} injection. A maximum of eight samples were assayed together, including one WT control per assay run.

Ca^{2+} release from permeabilized cells
Cell medium was changed 1 to 2 hours before harvesting. Cells were detached with trypsin (Gibco, 12605-010) and resuspended in cell medium. One million HeLa cells or 0.5 million AML12 cells were centrifuged at 800*g* for 3 min. Cell pellets were washed with PBS (Thermo Fisher Scientific, 20012050), centrifuged at 800*g* for 3 min, and resuspended in 150 μl of KCl buffer. KCl buffer consists of 125 mM KCl (Sigma-Aldrich, 793590), 2 mM K$_2$HPO$_4$ (Sigma-Aldrich, P3786), 1 mM MgCl$_2$, (Sigma-Aldrich, M8266), and 20 mM Hepes (pH 7.2; Sigma-Aldrich, H3375) supplemented fresh with 1 μM Oregon Green 488 Bapta-6F (Invitrogen, O23990). Digitonin (0.01 or 0.005%; Thermo Fisher Scientific, BN2006) was added for HeLa and AML12 cell assays, respectively. Cells were transferred to a black 96-well plate (Greiner Bio-One, 655076). Fluorescence (Ex, 485/20 nm; and Em, 520/20 nm) was monitored every 2 s for 196 s at room temperature using a BioTek Synergy H1 microplate reader (Thermo Fisher Scientific, 11-120-536) before and after injection of 1 μM CCCP (Cayman Chemical Company, 25458) in KCl buffer at 12 sec. Ca^{2+} release was calculated using the absolute difference between fluorescence reads before CCCP injection (average of six values, 0 to 10 s) and 3 min after injection (average of six values, 186 to 196 s). A maximum of eight samples were assayed together, including one WT control per assay run. For PKA kinase inhibition assays, AML12 cells were cultured for 4 days with 5 μM BLU2864 or dimethyl sulfoxide vehicle control. Cells were passaged on day 2, and fresh medium and drug were added. Ca^{2+} release experiments with BLU2864 were performed with ~0.5 million cells; however, BLU2864-treated cells formed clumps and could not be counted precisely. Data were instead normalized

by protein concentration. Following Ca^{2+} release, 1 µl of Triton X-100 (Sigma-Aldrich, X100) was added to each well, and the solution was pipetted vigorously. Protein concentration was then determined by Bradford assay (Bio-Rad, 5000205).

TEM of FLC patient liver

Tissue fixation was performed with 4% glutaraldehyde in 0.1 M sodium cacodylate buffer and then stored overnight at 4°C. The tissue was then washed five times for 5 min in buffer at room temperature and postfixed in buffered 2% osmium tetroxide on ice for 1 hour. This was followed by five washes in ddH_2O and then en bloc staining in 1% uranyl acetate (aqueous), overnight at 4°C. The following day the tissue was washed five times for 5 min in ddH_2O then dehydrated in ice-cold 30, 50, 70, and 95% ethanol and then allowed to come to room temperature. This was followed by 2 changes of 100% ethanol and two changes of propylene oxide. The tissue was then infiltrated in a 1:1 mixture of propylene oxide:Epon Araldite resin for 2 hours followed by two changes of fresh Epon Araldite, 2 hours each change. It was then placed in flat embedding molds and polymerized at 60°C overnight. Fixed samples were sliced to a thickness of 80 nm and were imaged on a JEOL1230 transmission electron microscope (TEM) operated at 80 kV.

Quantification of mitochondria and deposits from EM images

Images of patient liver tissue taken at ×10,000 magnification were analyzed by two independent, blinded researchers. First, mitochondria were identified in each image. Mitochondria were characterized as structures with a well-defined, curved border, typically 0.5 to 1 µm in diameter, with a mottled, gray matrix and at least one visible cristae line. Confirmed mitochondria were examined for the presence or absence of black, electron-dense deposits. Deposits were defined as speckles that were both darker and thicker in diameter than cristae membrane lines. With FLC patient 42.2, for which no NTL sample was available, cells from the tumor periphery were classified as oncocytic or peri-oncocytic. Cells with a circular nucleus and dispersed mitochondria were classified as peri-oncocytic; cells with misshapen nuclei and abundant cytoplasmic mitochondria were classified as oncocytic.

TMRM measurements

A total of 500,000 AML12 cells were centrifuged at 800g for 3 min, washed with 1 ml of PBS (Thermo Fisher Scientific, 20012050), and centrifuged again at 800g for 3 min. The supernatant was aspirated, and the cell pellet was resuspended in 150 µl of KCl buffer (for composition, see the "Ca^{2+} uptake in permeabilized cells" section) supplemented with 500 nM tetramethylrhodamine methyl ester (TMRM; Thermo Fisher Scientific, I34361) and 0.005% digitonin (Thermo Fisher Scientific, BN2006). The cell suspension was transferred to a black 96-well plate (Greiner Bio-One, 655076). Fluorescence measurements (Ex, 540 nm; and Em, 590 nm) were taken across three periods using a BioTek Synergy H1 microplate reader (Thermo Fisher Scientific, 11-120-536). The first measurements were taken every second for 1 min to establish a baseline. Then, 500 mM glutamate (Sigma-Aldrich, G1251) and 5 mM malate (Sigma-Aldrich, M7397) stocks were injected for final concentrations of 5 mM, and a second reading was taken every second for 1 min to obtain the minimum fluorescence, corresponding with maximal mitochondrial membrane potential. Last, mitochondrial membrane potential was dissipated

with the addition of 1 µM CCCP (Cayman Chemical Company, 25458), and reads were taken every second for 2 min to obtain the maximum fluorescence. Relative mitochondrial membrane potential was reported as the difference between the maximum (average of data from 294 to 304 s) and minimum TMRM fluorescence measurements (average of data from 172 to 182 s).

Generation of mito-G-GECO constructs and matrix and cytosolic Ca^{2+} measurements

The pLMM1 vector was generated from pLYS1 (86) by replacing the CMV promoter with the EF1α promoter. G-GECO1.1 (47) was cloned into either pLYS1 or pLMM1 with an N-terminal mitochondrial targeting sequence taken from cytochrome C subunit 8A (COX8). AML12 cells were transduced with mito-G-GECO lentiviral constructs generated using pLYS1 (WT and c14) or pLMM1 (c4) and selected with puromycin as described above. A total of 80,000 AML12 WT, c14, and c4 cells expressing mito-G-GECO were cultured in 12-well plates for 2 days until reaching 90 to 95% confluency. Medium was then aspirated and replaced with 500 µl of phenol red–free DMEM/F-12 (Thermo Fisher Scientific, 21041025) supplemented with 10% FBS (VWR, 89510-186) and penicillin (100 IU/ml) and streptomycin (100 µg/ml; VWR, 45000-652) for 1.5 hours. Fluorescence measurements (Ex, 480 nm; and Em, 520 nm) were obtained with a BioTek Synergy H1 microplate reader (Thermo Fisher Scientific, 11-120-536) at 37°C. To establish baseline, fluorescence was measured every 10 s for 2 min. Then, CCCP was added to a final concentration of 50 µM (Cayman Chemical Company, 25458) to each well, and fluorescence was measured to determine minimum fluorescence. Last, 5 µl of 1 mM stock of ionomycin (Sigma-Aldrich, I3909) and 10 µl of 1 M stock of $CaCl_2$ were added, and fluorescence was measured to establish maximum fluorescence. To correct for potential differences in mito-G-GECO expression across cell lines, baseline results were reported as a percentage of the difference between maximum and minimum values. To calculate the baseline fraction, minimum fluorescence is subtracted from baseline fluorescence over minimum fluorescence subtracted from maximum fluorescence. For each measurement, baseline, minimum, and maximum values were determined manually.

AML12 cells were transduced with cyto-G-GECO lentiviral constructs generated using pLYS1 and selected with puromycin as described above. Twelve-well plates were coated with EmbryoMax 0.1% Gelatin Solution (Sigma-Aldrich, ES-006) for 10 min. Excess gelatin solution was aspirated off, and 80,000 AML12 WT, c14, and c4 cells expressing cyto-G-GECO were cultured in the 12-well plates for 2 days until reaching 90 to 95% confluency. Medium was then aspirated and replaced with 500 µl of phenol red–free DMEM/F-12 (Thermo Fisher Scientific, 21041025) supplemented with 10% FBS (VWR, 89510-186) and penicillin (100 IU/ml) and streptomycin (100 µg/ml; VWR, 45000-652) for 1.5 hours. Fluorescence measurements (Ex, 480 nm; and Em, 520 nm) were obtained with a BioTek Synergy H1 microplate reader (Thermo Fisher Scientific, 11-120-536) at 37°C. To establish baseline, fluorescence was measured every 10 s for 2 min. Then, 5 µM ionomycin (Sigma-Aldrich, I3909) and 2.5 µM EGTA (Sigma-Aldrich, E3889) were added to each well, and fluorescence was measured to determine minimum fluorescence. Last, 10 µM $CaCl_2$ was added, and fluorescence was measured to establish maximum fluorescence. To correct for potential differences in cyto-G-GECO expression across cell lines, baseline results were reported as a percentage of the difference between maximum and minimum values. To calculate the baseline fraction, minimum fluorescence is

subtracted from baseline fluorescence over minimum fluorescence subtracted from maximum fluorescence. For each measurement, baseline, minimum, and maximum values were determined manually.

$^{13}C_6$ leucine carbon tracing

A total of 800,000 Hela WT and MCU KO cells were plated in two six-well plates to achieve 85 to 95% confluency. The next day, one plate was taken and washed twice with PBS (Thermo Fisher Scientific, 20012050), and the medium was changed to DMEM/F-12 without amino acids [US Biological, D9807-02A; prepared with sodium bicarbonate (84 g/mol), Hepes (238 g/mol), and glucose (180 g/mol) (pH to 7.2)] mixed with 10 mM L-leucine-$^{13}C_6$ (MedChem Express, HY-N0486S2). This DMEM/F-12 without glucose or amino acids was supplemented with dialyzed 10% FBS (VWR, 89510-186), 1× insulin-transferrin-selenium (Gibco, 41400045), dexamethasone (40 ng/ml; MP Biomedicals, 0219456180), and penicillin (100 IU/ml) and streptomycin (100 μg/ml; VWR, 45000-652) and all amino acid (except leucine) concentrations matching that of DMEM/F-12 (Thermo Fisher Scientific, 21041025). FBS dialysis was done with Slide-A-Lyzer Dialysis Flasks (Thermo Fisher Scientific, 87761) to 3.5 kDa. This plate was then left to incubate in 37°C with 5% CO_2 for 2 hours to ensure that L-leucine-13C6 was incorporated. The plate was then quickly washed with 1× HPLC-grade ice-cold saline (Thermo Fisher Scientific, 23293184) which was aspirated before adding 500 μl of ice-cold 80% HPLC-grade methanol (Sigma-Aldrich, 646377) in HPLC-grade water (Sigma-Aldrich, 270733). Each well was quickly scraped using a cell scraper to disrupt the cell layer, quenching metabolism and preventing substantial amounts of evaporation. Depending on evaporation, 400 to 500 μl of liquid in each well was transferred to a microcentrifuge tube, and this was centrifuged at 17,000g for 10 min at 4°C. As much of the same amount of supernatant was then taken from each and transferred to a new microcentrifuge tube, and this was centrifuged again at 17,000g for 10 min at 4°C. Last, 350 μl of the supernatant of each sample was transferred to a new microcentrifuge tube and lyophilized. After collection, the second six-well plate was taken and counted using a Coulter Z2 Cell and Particle Counter (Beckman Coulter, 383550) to obtain cell counts for normalization of each sample.

Liquid chromatography–mass spectrometry

Lyophilized samples were resuspended in 80% HPLC grade methanol in HPLC grade water and transferred to LCMS vials for measurement by LCMS. Metabolite quantitation was performed using a Q Exactive HF-X Hybrid Quadrupole-Orbitrap Mass Spectrometer equipped with an Ion Max API source and H-ESI II probe, coupled to a Vanquish Flex Binary UHPLC system (Thermo Fisher Scientific). Mass calibrations were completed at a minimum of every 5 days in both the positive and negative polarity modes using LTQ Velos ESI Calibration Solution (Pierce). Polar Samples were chromatographically separated by injecting a sample volume of 1 μl into a SeQuant ZIC-pHILIC Polymeric column (2.1 mm by 150 mm 5 mM, EMD Millipore). The flow rate was set to 150 ml/min, autosampler temperature was set to 10°C, and column temperature was set to 30°C. Mobile phase A consisted of 20 mM ammonium carbonate and 0.1% (v/v) ammonium hydroxide, and mobile phase B consisted of 100% acetonitrile. The sample was gradient eluted (% B) from the column as follows: 0 to 20 min: linear gradient from 85 to 20% B; 20 to 24 min: hold at 20% B; 24 to 24.5 min: linear gradient from 20 to 85% B; 24.5 min until the end: hold at 85% B until equilibrated with

ten column volumes. Mobile phase was directed into the ion source with the following parameters: sheath gas, 45; auxiliary gas, 15; sweep gas, 2; spray voltage, 2.9 kV in the negative mode or 3.5 kV in the positive mode; capillary temperature, 300°C; RF level, 40%; and auxiliary gas heater temperature, 325°C. Mass detection was conducted with a resolution of 240,000 in full scan mode, with an AGC target of 3,000,000 and maximum injection time of 250 ms. Metabolites were detected over a mass range of 70 to 1050 m/z. Quantitation of all metabolites was performed using Tracefinder 4.1 (Thermo Fisher Scientific) referencing an in-house metabolite standards library using ≤5–part-per-million mass error. Data from leucine isotope labeling experiments include correction for natural isotope abundance using IsoCor software v.2.2.

NADH/NAD$^+$ measurements

A total of 20,000 Hela WT and MCU KO cells were plated in six-well plates with DMEM (Thermo Fisher Scientific, 11-965-118) supplemented with 10% FBS (VWR, 89510-186), 2 mM GlutaMAX (Thermo Fisher Scientific, 35-050-061), penicillin (100 IU/ml), and streptomycin (100 μg/ml; VWR, 45000-652) and allowed to adhere overnight. The medium was aspirated and cells were rinsed with PBS (Thermo Fisher Scientific, 20012050) and replaced with DMEM:F12 without glucose and amino acids (US Biological, D9807-02A), which was supplemented with dialyzed 10% FBS, penicillin (100 IU/ml) and streptomycin (100 μg/ml), glucose, and either non-BCAAs or all amino acids. Plates were incubated for 3 hours. at 37°C in 5% CO_2. Cells were washed three times in ice-cold PBS. They were then extracted in 100 μl of ice-cold lysis buffer [1% dodecyltrimethylammonium bromide (DTAB) in 0.2 N of NaOH diluted 1:1 with PBS] and immediately frozen at −80°C and kept there until all replicates were collected. For NADH measurement, 40 μl of freshly thawed lysates was transferred to microcentrifuge tubes and incubated at 75°C for 30 min for base-mediated degradation of NAD$^+$. For NAD$^+$ measurement, 40 μl of lysis buffer was added with 40 μl of 0.4 N HCl and 40 μl of freshly thawed lysate in microcentrifuge tube. This was then incubated at 60°C for 15 min for acidic conditions to selectively degrade NADH. After respective incubations, samples were allowed to equilibrate to room temperature for 8 min. NADH measurement samples were quenched with 40 μl of 0.25 M tris in 0.2 N HCl. NAD$^+$ measurement samples were quenched with 40 μl of 0.5 M tris base. Stocks (0, 10, 100, 200, and 400 nM) were prepared right before running the assay by diluting 1 μM NAD$^+$ in a mixture of equal volumes of PBS, base solution with 1% DTAB, 0.4 N HCl, and 0.5 M Trizma base. The working reagent (reconstituted luciferan detection reagent, reductase, reductase substrate, NAD$^+$ cycling enzyme, and NAD cycling substrate) added to the NADH and NAD$^+$ samples were prepared using the instructions provided by the NAD$^+$/NADH Glo Assay Kit (Promega, G9071). Sample or standard solution (1:1) and working reagent from kit were added to a plate using multichannel pipette. Enzyme-linked luminescence–based NAD$^+$ and NADH measurement were measured at 0 and 40 min using the BioTek Synergy H1 plate reader (Thermo Fisher Scientific, 11-120-536). Luminescence readings of NAD$^+$ and NADH were used to calculate the NADH/NAD$^+$ ratio and subsequent fold changes.

Analysis of gene expression

Raw data files (FASTQ format) were downloaded from the European Nucleotide Archive for each GEO study. Counts per gene were computed from the FASTQ files by first aligning to the NCBI GRCh38

transcriptome using the salmon aligner (*87*) and then collapsing to the gene level using the Bioconductor tximport package (*88*). The Bioconductor edgeR (*89*) package was then used to fit linear models for each study using the limma-voom pipeline (*88*) and then computing empirical Bayes adjusted contrasts (*90*) between FLC and normal liver. For those datasets with complete pairing, the linear model included a blocking effect for patient, and, for those with only partial pairing, a linear mixed-effects model was fit to account for within-patient correlation. A meta-analysis was then performed using Stouffer's method (*91*), implemented in the Bioconductor metapod package (*92*), using the inverse of the effect size as weights to improve precision (*93*).

Preparation of medium with different BCAA concentrations

For the 100% BCAA condition, DMEM/F-12 without glucose or amino acids (US Biological, D9807-02A) was supplemented with glucose (180 g/mol), Hepes (238 g/mol), sodium bicarbonate (84 g/mol), dialyzed 10% FBS (VWR, 89510-186), 1× insulin-transferrin-selenium (Gibco, 41400045), dexamethasone (40 ng/ml; MP Biomedicals, 0219456180), penicillin (100 IU/ml), and streptomycin (100 µg/ml; VWR, 45000-652) and all amino acid concentrations matching DMEM/F-12 (Thermo Fisher Scientific, 21041025) (pH 7.2). FBS dialysis was done with Slide-A-Lyzer Dialysis Flasks (Thermo Fisher Scientific, 87761) to 3.5 kDa. The 30 and 50% BCAA condition combined the 100% BCAA DMEM:F12 medium with the 0% BCAA DMEM:F12 medium in the appropriate ratios. To make the 0% BCAA DMEM:F12 medium, the DMEM/F-12 without glucose or amino acids was supplemented with the same reagents but excluded BCAAs.

Growth assays using crystal violet staining

The medium was aspirated and 1× PBS (Thermo Fisher Scientific, 20012050) was gently pipetted into each well, ensuring that the cells were not disturbed. The PBS was aspirated and 4% paraformaldehyde (PFA) (Thermo Fisher Scientific, 50-980-487) in PBS was added for 10 min to fix the cells. After removing the PFA, each well was gently washed twice with 1× PBS again. Then, 0.1% crystal violet stain (Thermo Fisher Scientific, AAB2193214) dissolved in 10% MeOH (MilliporeSigma, 32213) was added to each well and left to incubate at room temperature for 20 min. After removing the crystal violet stain, each well was gently washed twice with ddH$_2$O. Last, ddH$_2$O was added for 5 min to ensure that residual crystal violet dye not bound to cells was washed out. The ddH$_2$O was aspirated and the 12-well plate was left overturned to dry completely. Once each well was completely dry, the absorbance of each well was read with BioTek Synergy H1 microplate reader (Thermo Fisher Scientific, 11-120-536) at 590 nm. The average absorbance of each well was then calculated.

Supplementary Materials
This PDF file includes:
Figs. S1 to S6
Table S1

REFERENCES AND NOTES

1. E. Balderas, D. R. Eberhardt, S. Lee, J. M. Pleinis, S. Sommakia, A. M. Balynas, X. Yin, M. C. Parker, C. T. Maguire, S. Cho, M. W. Szulik, A. Bakhtina, R. D. Bia, M. W. Friederich, T. M. Locke, J. L. K. van Hove, S. G. Drakos, Y. Sancak, M. Tristani-Firouzi, S. Franklin, A. R. Rodan, D. Chaudhuri, Mitochondrial calcium uniporter stabilization preserves energetic homeostasis during complex I impairment. *Nat. Commun.* **13**, 2769 (2022).

2. G. Gherardi, L. Nogara, S. Ciciliot, G. P. Fadini, B. Blaauw, P. Braghetta, P. Bonaldo, D. de Stefani, R. Rizzuto, C. Mammucari, Loss of mitochondrial calcium uniporter rewires skeletal muscle metabolism and substrate preference. *Cell Death Differ.* **26**, 362–381 (2019).

3. J. Huo, J. D. Molkentin, MCU genetically altered mice suggest how mitochondrial Ca^{2+} regulates metabolism. *Trends Endocrinol. Metab.* **35**, 918–928 (2024).

4. J. Q. Kwong, J. Huo, M. J. Bround, J. G. Boyer, J. A. Schwanekamp, N. Ghazal, J. T. Maxwell, Y. C. Jang, Z. Khuchua, K. Shi, D. M. Bers, J. Davis, J. D. Molkentin, The mitochondrial calcium uniporter underlies metabolic fuel preference in skeletal muscle. *JCI Insight* **3**, e121689 (2018).

5. D. Tomar, J. W. Elrod, Metabolite regulation of the mitochondrial calcium uniporter channel. *Cell Calcium* **92**, 102288 (2020).

6. J. M. Baughman, F. Perocchi, H. S. Girgis, M. Plovanich, C. A. Belcher-Timme, Y. Sancak, X. R. Bao, L. Strittmatter, O. Goldberger, R. L. Bogorad, V. Koteliansky, V. K. Mootha, Integrative genomics identifies MCU as an essential component of the mitochondrial calcium uniporter. *Nature* **476**, 341–345 (2011).

7. D. De Stefani, A. Raffaello, E. Teardo, I. Szabò, R. Rizzuto, A forty-kilodalton protein of the inner membrane is the mitochondrial calcium uniporter. *Nature* **476**, 336–340 (2011).

8. M. J. S. MacEwen, Y. Sancak, Beyond the matrix: Structural and physiological advancements in mitochondrial calcium signaling. *Biochem. Soc. Trans.* **51**, 665–673 (2023).

9. M. Plovanich, R. L. Bogorad, Y. Sancak, K. J. Kamer, L. Strittmatter, A. A. Li, H. S. Girgis, S. Kuchimanchi, J. de Groot, L. Speciner, N. Taneja, J. OShea, V. Koteliansky, V. K. Mootha, MICU2, a paralog of MICU1, resides within the mitochondrial uniporter complex to regulate calcium handling. *PLOS ONE* **8**, e55785 (2013).

10. Y. Sancak, A. L. Markhard, T. Kitami, E. Kovács-Bogdán, K. J. Kamer, N. D. Udeshi, S. A. Carr, D. Chaudhuri, D. E. Clapham, A. A. Li, S. E. Calvo, O. Goldberger, V. K. Mootha, EMRE is an essential component of the mitochondrial calcium uniporter complex. *Science* **342**, 1379–1382 (2013).

11. G. Csordas, T. Golenár, E. L. Seifert, K. J. Kamer, Y. Sancak, F. Perocchi, C. Moffat, D. Weaver, S. de la Fuente Perez, R. Bogorad, V. Koteliansky, J. Adijanto, V. K. Mootha, G. Hajnóczky, MICU1 controls both the threshold and cooperative activation of the mitochondrial Ca^{2+} uniporter. *Cell Metab.* **17**, 976–987 (2013).

12. E. Kovacs-Bogdan, Y. Sancak, K. J. Kamer, M. Plovanich, A. Jambhekar, R. J. Huber, M. A. Myre, M. D. Blower, V. K. Mootha, Reconstitution of the mitochondrial calcium uniporter in yeast. *Proc. Natl. Acad. Sci. U.S.A.* **111**, 8985–8990 (2014).

13. J. C. Liu, J. Liu, K. M. Holmström, S. Menazza, R. J. Parks, M. M. Fergusson, Z. X. Yu, D. A. Springer, C. Halsey, C. Liu, E. Murphy, T. Finkel, MICU1 serves as a molecular gatekeeper to prevent in vivo mitochondrial calcium overload. *Cell Rep.* **16**, 1561–1573 (2016).

14. M. Patron, H.-G. Sprenger, T. Langer, m-AAA proteases, mitochondrial calcium homeostasis and neurodegeneration. *Cell Res.* **28**, 296–306 (2018).

15. A. P. Arruda, B. M. Pers, G. Parlakgül, E. Güney, K. Inouye, G. S. Hotamisligil, Chronic enrichment of hepatic endoplasmic reticulum-mitochondria contact leads to mitochondrial dysfunction in obesity. *Nat. Med.* **20**, 1427–1435 (2014).

16. T. König, S. E. Tröder, K. Bakka, A. Korwitz, R. Richter-Dennerlein, P. A. Lampe, M. Patron, M. Mühlmeister, S. Guerrero-Castillo, U. Brandt, T. Decker, I. Lauria, A. Paggio, R. Rizzuto, E. I. Rugarli, D. De Stefani, T. Langer, The m-AAA protease associated with neurodegeneration limits MCU activity in mitochondria. *Mol. Cell* **64**, 148–162 (2016).

17. G. C. Walters, Y. M. Usachev, Mitochondrial calcium cycling in neuronal function and neurodegeneration. *Front. Cell Dev. Biol.* **11**, 1094356 (2023).

18. S. Ghosh, M. Zulkifli, A. Joshi, M. Venkatesan, A. Cristel, N. Vishnu, M. Madesh, V. M. Gohil, MCU-complex-mediated mitochondrial calcium signaling is impaired in Barth syndrome. *Hum. Mol. Genet.* **31**, 376–385 (2022).

19. S. Marchi, C. Giorgi, L. Galluzzi, P. Pinton, Ca^{2+} fluxes and cancer. *Mol. Cell* **78**, 1055–1069 (2020).

20. E. Fernandez Garcia, U. Paudel, M. C. Noji, C. E. Bowman, A. K. Rustgi, J. R. Pitarresi, K. E. Wellen, Z. Arany, J. S. Weissenrieder, J. K. Foskett, The mitochondrial Ca^{2+} channel MCU is critical for tumor growth by supporting cell cycle progression and proliferation. *Front Cell Dev. Biol.* **11**, 1082213 (2023).

21. O. M. Koval, E. K. Nguyen, V. Santhana, T. P. Fidler, S. C. Sebag, T. P. Rasmussen, D. J. Mittauer, S. Strack, P. C. Goswami, E. D. Abel, I. M. Grumbach, Loss of MCU prevents mitochondrial fusion in G$_1$-S phase and blocks cell cycle progression and proliferation. *Sci. Signal.* **12**, eaav1439 (2019).

22. H. Zhao, T. Li, K. Wang, F. Zhao, J. Chen, G. Xu, J. Zhao, T. Li, L. Chen, L. Li, Q. Xia, T. Zhou, H.-Y. Li, A.-L. Li, T. Finkel, X.-M. Zhang, X. Pan, AMPK-mediated activation of MCU stimulates mitochondrial Ca^{2+} entry to promote mitotic progression. *Nat. Cell Biol.* **21**, 476–486 (2019).

23. J. C. Liu, N. C. Syder, N. S. Ghorashi, T. B. Willingham, R. J. Parks, J. Sun, M. M. Fergusson, J. Liu, K. M. Holmström, S. Menazza, D. A. Springer, C. Liu, B. Glancy, T. Finkel, E. Murphy, EMRE is essential for mitochondrial calcium uniporter activity in a mouse model. *JCI Insight* **5**, e134063 (2020).

24. X. Pan, J. Liu, T. Nguyen, C. Liu, J. Sun, Y. Teng, M. M. Fergusson, I. I. Rovira, M. Allen, D. A. Springer, A. M. Aponte, M. Gucek, R. S. Balaban, E. Murphy, T. Finkel, The physiological role of mitochondrial calcium revealed by mice lacking the mitochondrial calcium uniporter. *Nat. Cell Biol.* **15**, 1464–1472 (2013).

25. A. A. Lombardi, A. A. Gibb, E. Arif, D. W. Kolmetzky, D. Tomar, T. S. Luongo, P. Jadiya, E. K. Murray, P. K. Lorkiewicz, G. Hajnóczky, E. Murphy, Z. P. Arany, D. P. Kelly, K. B. Margulies, B. G. Hill, J. W. Elrod, Mitochondrial calcium exchange links metabolism with the epigenome to control cellular differentiation. *Nat. Commun.* **10**, 4509 (2019).

26. T. M. Bauer, E. Murphy, Role of mitochondrial calcium and the permeability transition pore in regulating cell death. *Circ. Res.* **126**, 280–293 (2020).

27. J. R. Craig, R. L. Peters, H. A. Edmondson, M. Omata, Fibrolamellar carcinoma of the liver: A tumor of adolescents and young adults with distinctive clinico-pathologic features. *Cancer* **46**, 372–379 (1980).

28. D. C. Farhi, R. H. Shikes, S. G. Silverberg, Ultrastructure of fibrolamellar oncocytic hepatoma. *Cancer* **50**, 702–709 (1982).

29. J. Lloreta, C. Vadell, X. Fabregat, S. Serrano, Fibrolamellar hepatic tumor with neurosecretory features and systemic deposition of AA amyloid. *Ultrastruct. Pathol.* **18**, 287–292 (1994).

30. S. N. Levin, M. D. Tomasini, J. Knox, M. Shirani, B. Shebl, D. Requena, J. Clark, S. Heissel, H. Alwaseem, R. Surjan, R. Lahasky, H. Molina, M. S. Torbenson, B. Lyons, R. D. Migler, P. Coffino, S. M. Simon, Disruption of proteome by an oncogenic fusion kinase alters metabolism in fibrolamellar hepatocellular carcinoma. *Sci. Adv.* **9**, eadg7038 (2023).

31. D. Jeyaraj, F. A. J. L. Scheer, J. A. Ripperger, S. M. Haldar, Y. Lu, D. A. Prosdocimo, S. J. Eapen, B. L. Eapen, Y. Cui, G. H. Mahabeleshwar, H. G. Lee, M. A. Smith, G. Casadesus, E. M. Mintz, H. Sun, Y. Wang, K. M. Ramsey, J. Bass, S. A. Shea, U. Albrecht, M. K. Jain, Klf15 orchestrates circadian nitrogen homeostasis. *Cell Metab.* **15**, 311–323 (2012).

32. N. Thakral, D. A. Simonetto, Hyperammonemic encephalopathy: An unusual presentation of fibrolamellar hepatocellular carcinoma. *Clin. Mol. Hepatol.* **26**, 74–77 (2020).

33. D. Long Jr., M. Chan, M. Han, Z. Kamdar, R. K. Ma, P. Y. Tsai, A. B. Francisco, J. Barrow, D. B. Shackelford, M. Yarchoan, M. J. McBride, L. M. Orre, N. M. Vacanti, T. S. Gujral, P. Sethupathy, Proteo-metabolomics and patient tumor slice experiments point to amino acid centrality for rewired mitochondria in fibrolamellar carcinoma. *Cell Rep. Med.* **5**, 101699 (2024).

34. M. P. Young, Z. T. Schug, D. M. Booth, D. I. Yule, K. Mikoshiba, G. Hajnóczky, S. K. Joseph, Metabolic adaptation to the chronic loss of Ca^{2+} signaling induced by KO of IP_3 receptors or the mitochondrial Ca^{2+} uniporter. *J. Biol. Chem.* **298**, 101436 (2022).

35. B. Glancy, R. S. Balaban, Role of mitochondrial Ca^{2+} in the regulation of cellular energetics. *Biochemistry* **51**, 2959–2973 (2012).

36. S. X. Ge, D. Jung, R. Yao, ShinyGO: A graphical gene-set enrichment tool for animals and plants. *Bioinformatics* **36**, 2628–2629 (2020).

37. B. Huang, R. Gudi, P. Wu, R. A. Harris, J. Hamilton, K. M. Popov, Isoenzymes of pyruvate dehydrogenase phosphatase. DNA-derived amino acid sequences, expression, and regulation. *J. Biol. Chem.* **273**, 17680–17688 (1998).

38. E. Pezzato, V. Battaglia, A. M. Brunati, E. Agostinelli, A. Toninello, Ca^{2+} −independent effects of spermine on pyruvate dehydrogenase complex activity in energized rat liver mitochondria incubated in the absence of exogenous Ca^{2+} and Mg^{2+}. *Amino Acids* **36**, 449–456 (2009).

39. A. Acevedo, A. E. Jones, B. T. Danna, R. Turner, K. P. Montales, C. Benincá, K. Reue, O. S. Shirihai, L. Stiles, M. Wallace, Y. Wang, A. M. Bertholet, A. S. Divakaruni, The BCKDK inhibitor BT2 is a chemical uncoupler that lowers mitochondrial ROS production and de novo lipogenesis. *J. Biol. Chem.* **300**, 105702 (2024).

40. M. Neinast, D. Murashige, Z. Arany, Branched chain amino acids. *Annu. Rev. Physiol.* **81**, 139–164 (2019).

41. J. N. Honeyman, E. P. Simon, N. Robine, R. Chiaroni-Clarke, D. G. Darcy, I. I. P. Lim, C. E. Gleason, J. M. Murphy, B. R. Rosenberg, L. Teegan, C. N. Takacs, S. Botero, R. Belote, S. Germer, A. K. Emde, V. Vacic, U. Bhanot, M. P. LaQuaglia, S. M. Simon, Detection of a recurrent DNAJB1-PRKACA chimeric transcript in fibrolamellar hepatocellular carcinoma. *Science* **343**, 1010–1014 (2014).

42. G. Gasparre, G. Romeo, M. Rugolo, A. M. Porcelli, Learning from oncocytic tumors: Why choose inefficient mitochondria? *Biochim. Biophys. Acta* **1807**, 633–642 (2011).

43. S. G. Wolf, Y. Mutsafi, T. Dadosh, T. Ilani, Z. Lansky, B. Horowitz, S. Rubin, M. Elbaum, D. Fass, 3D visualization of mitochondrial solid-phase calcium stores in whole cells. *eLife* **6**, e29929 (2017).

44. J. O. Strubbe-Rivera, J. R. Schrad, E. V. Pavlov, J. F. Conway, K. N. Parent, J. N. Bazil, The mitochondrial permeability transition phenomenon elucidated by cryo-EM reveals the genuine impact of calcium overload on mitochondrial structure and function. *Sci. Rep.* **11**, 1037 (2021).

45. R. E. Turnham, F. D. Smith, H. L. Kenerson, M. H. Omar, M. Golkowski, I. Garcia, R. Bauer, H.-T. Lau, K. M. Sullivan, L. K. Langeberg, S.-E. Ong, K. J. Riehle, R. S. Yeung, J. D. Scott, An acquired scaffolding function of the DNAJ-PKAc fusion contributes to oncogenic signaling in fibrolamellar carcinoma. *eLife* **8**, e44187 (2019).

46. T. A. Dinh, R. Sritharan, F. D. Smith, A. B. Francisco, R. K. Ma, R. P. Bunaciu, M. Kanke, C. G. Danko, A. P. Massa, J. D. Scott, P. Sethupathy, Hotspots of aberrant enhancer activity in fibrolamellar carcinoma reveal candidate oncogenic pathways and therapeutic vulnerabilities. *Cell Rep.* **31**, 107509 (2020).

47. Y. Zhao, S. Araki, J. Wu, T. Teramoto, Y. F. Chang, M. Nakano, A. S. Abdelfattah, M. Fujiwara, T. Ishihara, T. Nagai, R. E. Campbell, An expanded palette of genetically encoded Ca^{2+} indicators. *Science* **333**, 1888–1891 (2011).

48. C. Neumayer, D. Ng, C. S. Jiang, A. Qureshi, G. Lalazar, R. Vaughan, S. M. Simon, Oncogenic addiction of fibrolamellar hepatocellular carcinoma to the fusion kinase DNAJB1-PRKACA. *Clin. Cancer Res.* **29**, 271–278 (2023).

49. A. Toyota, M. Goto, M. Miyamoto, S. Nagashima, S. Iwasaki, T. Komatsu, T. Momose, K. Yoshida, T. Tsukada, T. Matsufuji, A. Ohno, M. Suzuki, O. Ubukata, Y. Kaneta, Novel protein kinase cAMP-Activated Catalytic Subunit Alpha (PRKACA) inhibitor shows anti-tumor activity in a fibrolamellar hepatocellular carcinoma model. *Biochem. Biophys. Res. Commun.* **621**, 157–161 (2022).

50. M. I. Davis, J. P. Hunt, S. Herrgard, P. Ciceri, L. M. Wodicka, G. Pallares, M. Hocker, D. K. Treiber, P. P. Zarrinkar, Comprehensive analysis of kinase inhibitor selectivity. *Nat. Biotechnol.* **29**, 1046–1051 (2011).

51. J. F. Garbincius, T. S. Luongo, J. P. Lambert, A. S. Mangold, E. K. Murray, A. N. Hildebrand, P. Jadiya, J. W. Elrod, MCU gain- and loss-of-function models define the duality of mitochondrial calcium uptake in heart failure. bioRxiv 537222 [Preprint] (2023).

52. R. E. Ericksen, S. L. Lim, E. McDonnell, W. H. Shuen, M. Vadiveloo, P. J. White, Z. Ding, R. Kwok, P. Lee, G. K. Radda, H. C. Toh, M. D. Hirschey, W. Han, Loss of BCAA catabolism during carcinogenesis enhances mTORC1 activity and promotes tumor development and progression. *Cell Metab.* **29**, 1151–1165.e6 (2019).

53. M. M. Bowker-Kinley, W. I. Davis, P. Wu, R. A. Harris, K. M. Popov, Evidence for existence of tissue-specific regulation of the mammalian pyruvate dehydrogenase complex. *Biochem. J.* **329**, 191–196 (1998).

54. N. Grankvist, C. Jönsson, K. Hedin, N. Sundqvist, P. Sandström, B. Björnsson, A. Begzati, E. Mickols, P. Artursson, M. Jain, G. Cedersund, R. Nilsson, Global ^{13}C tracing and metabolic flux analysis of intact human liver tissue ex vivo. *Nat. Metab.* **6**, 1963–1975 (2024).

55. I. Gritti, J. Wan, V. Weeresekara, J. M. Vaz, G. Tarantino, T. H. Bryde, V. Vijay, A. V. Kammula, P. Kattel, S. Zhu, P. Vu, M. Chan, M. J. Wu, J. D. Gordan, K. C. Patra, V. S. Silveira, R. T. Manguso, M. N. Wein, C. J. Ott, J. Qi, D. Liu, K. Sakamoto, T. S. Gujral, N. Bardeesy, DNAJB1-PRKACA fusion drives fibrolamellar liver cancer through impaired SIK signaling and CRTC2/p300-mediated transcriptional reprogramming. *Cancer Discov.* **15**, 382–400 (2025).

56. H. Chen, L.-L. Li, Y. Du, Kruppel-like factor 15 in liver diseases: Insights into metabolic reprogramming. *Front. Pharmacol.* **14**, 1115226 (2023).

57. D. Shao, O. Villet, Z. Zhang, S. W. Choi, J. Yan, J. Ritterhoff, H. Gu, D. Djukovic, D. Christodoulou, S. C. Kolwicz Jr., D. Raftery, R. Tian, Glucose promotes cell growth by suppressing branched-chain amino acid degradation. *Nat. Commun.* **9**, 2935 (2018).

58. A. Auron, P. D. Brophy, Hyperammonemia in review: Pathophysiology, diagnosis, and treatment. *Pediatr. Nephrol.* **27**, 207–222 (2012).

59. E. K. K. Lo, Felicianna, J.-H. Xu, Q. Zhan, Z. Zeng, H. el-Nezami, The emerging role of branched-chain amino acids in liver diseases. *Biomedicine* **10**, 1444 (2022).

60. G. Mann, S. Mora, G. Madu, O. A. J. Adegoke, Branched-chain amino acids: Catabolism in skeletal muscle and implications for muscle and whole-body metabolism. *Front. Physiol.* **12**, 702826 (2021).

61. Y. Xiong, L. Jiang, T. Li, Aberrant branched-chain amino acid catabolism in cardiovascular diseases. *Front Cardiovasc. Med.* **9**, 965899 (2022).

62. A. Barbul, Proline precursors to sustain Mammalian collagen synthesis. *J. Nutr.* **138**, 2021S–2024S (2008).

63. F. De Chiara, K. L. Thomsen, A. Habtesion, H. Jones, N. Davies, J. Gracia-Sancho, N. Manicardi, A. Hall, F. Andreola, H. L. Paish, L. H. Reed, A. A. Watson, J. Leslie, F. Oakley, K. Rombouts, R. P. Mookerjee, J. Mann, R. Jalan, Ammonia scavenging prevents progression of fibrosis in experimental nonalcoholic fatty liver disease. *Hepatology* **71**, 874–892 (2020).

64. D. Harada, S. Nagamachi, K. Aso, K. Ikeda, Y. Takahashi, M. Furuse, Oral administration of L-ornithine increases the content of both collagen constituting amino acids and polyamines in mouse skin. *Biochem. Biophys. Res. Commun.* **512**, 712–715 (2019).

65. L. Mao, L. Liu, T. Zhang, H. Qin, X. Wu, Y. Xu, Histone deacetylase 11 contributes to renal fibrosis by repressing KLF15 transcription. *Front. Cell Dev. Biol.* **8**, 235 (2020).

66. Y. Tian, Z. Wang, X. Zheng, W. Song, L. Cai, M. Rane, Y. Zhao, KLF15 negatively regulates cardiac fibrosis by which SDF-1β attenuates cardiac fibrosis in type 2 diabetic mice. *Toxicol. Appl. Pharmacol.* **427**, 115654 (2021).

67. B. Wang, S. M. Haldar, Y. Lu, O. A. Ibrahim, S. Fisch, S. Gray, A. Leask, M. K. Jain, The Kruppel-like factor KLF15 inhibits connective tissue growth factor (CTGF) expression in cardiac fibroblasts. *J. Mol. Cell. Cardiol.* **45**, 193–197 (2008).

68. R. W. McGarrah, P. J. White, Branched-chain amino acids in cardiovascular disease. *Nat. Rev. Cardiol.* **20**, 77–89 (2023).

69. H. Sun, K. C. Olson, C. Gao, D. A. Prosdocimo, M. Zhou, Z. Wang, D. Jeyaraj, J. Y. Youn, S. Ren, Y. Liu, C. D. Rau, S. Shah, O. Ilkayeva, W. J. Gui, N. S. William, R. M. Wynn, C. B. Newgard, H. Cai, X. Xiao, D. T. Chuang, P. C. Schulze, C. Lynch, M. K. Jain, Y. Wang, Catabolic defect of banched-chain amino acids promotes heart failure. *Circulation* **133**, 2038–2049 (2016).

70. Q. Kanyomse, X. le, J. Tang, F. Dai, Y. Mobet, C. Chen, Z. Cheng, C. Deng, Y. Ning, R. Yu, X. Zeng, T. Xiang, KLF15 suppresses tumor growth and metastasis in triple-negative breast cancer by downregulating CCL2 and CCL7. *Sci. Rep.* **12**, 19026 (2022).

71. N. Wang, Q.-X. Cao, J. Tian, L. Ren, H.-L. Cheng, S.-Q. Yang, Circular RNA MTO1 inhibits the proliferation and invasion of ovarian cancer cells through the miR-182-5p/KLF15 axis. *Cell Transplant.* **29**, 963689720943613 (2020).

72. X. Wang, J. Liu, S. Xi, X. Pan, X. Fang, Exploring the mechanism of KLF15 on the biological activity and autophagy of gastric cancer cells based on PI3K/Akt/Mtor signaling pathway. *Comb. Chem. High Throughput Screen.* **27**, 1515–1523 (2024).

73. Z. H. Wang, L.-L. Ye, X. Xiang, X.-S. Wei, Y.-R. Niu, W.-B. Peng, S.-Y. Zhang, P. Zhang, Q.-Q. Xue, H.-L. Wang, Y.-H. Du, Y. Liu, J.-Q. Ai, Q. Zhou, Circular RNA circFBXO7 attenuates non-small cell lung cancer tumorigenesis by sponging miR-296-3p to facilitate KLF15-mediated transcriptional activation of CDKN1A. *Transl Oncol.* **30**, 101635 (2023).

74. K. Y. Zhu, Y. Tian, Y.-X. Li, Q.-X. Meng, J. Ge, X.-C. Cao, T. Zhang, Y. Yu, The functions and prognostic value of Kruppel-like factors in breast cancer. *Cancer Cell Int.* **22**, 23 (2022).

75. C. X. Sun, B. J. Liu, Y. Su, G. W. Shi, Y. Wang, J. F. Chi, MiR-181a promotes cell proliferation and migration through targeting KLF15 in papillary thyroid cancer. *Clin. Transl. Oncol.* **24**, 66–75 (2022).

76. C.-J. Li, H.-Y. Lin, C.-J. Ko, J.-C. Lai, P.-Y. Chu, A novel biomarker driving poor-prognosis liver cancer: Overexpression of the mitochondrial calcium gatekeepers. *Biomedicine* **8**, 451 (2020).

77. T. Ren, J. Wang, H. Zhang, P. Yuan, J. Zhu, Y. Wu, Q. Huang, X. Guo, J. Zhang, L. Ji, J. Li, H. Zhang, H. Yang, J. Xing, MCUR1-mediated mitochondrial calcium signaling facilitates cell survival of hepatocellular carcinoma via reactive oxygen species-dependent P53 degradation. *Antioxid. Redox Signal.* **28**, 1120–1136 (2018).

78. T. Ren, H. Zhang, J. Wang, J. Zhu, M. Jin, Y. Wu, X. Guo, L. Ji, Q. Huang, H. Zhang, H. Yang, J. Xing, MCU-dependent mitochondrial Ca^{2+} inhibits NAD^+/SIRT3/SOD2 pathway to promote ROS production and metastasis of HCC cells. *Oncogene* **36**, 5897–5909 (2017).

79. S. M. Hutson, R. Wallin, T. R. Hall, Identification of mitochondrial branched chain aminotransferase and its isoforms in rat tissues. *J. Biol. Chem.* **267**, 15681–15686 (1992).

80. K. J. Rosenthal, J. D. Gordan, J. D. Scott, Protein kinase A and local signaling in cancer. *Biochem. J.* **481**, 1659–1677 (2024).

81. J. Rappsilber, M. Mann, Y. Ishihama, Protocol for micro-purification, enrichment, pre-fractionation and storage of peptides for proteomics using StageTips. *Nat. Protoc.* **2**, 1896–1906 (2007).

82. A. T. Kong, F. V. Leprevost, D. M. Avtonomov, D. Mellacheruvu, A. I. Nesvizhskii, MSFragger: Ultrafast and comprehensive peptide identification in mass spectrometry-based proteomics. *Nat. Methods* **14**, 513–520 (2017).

83. V. Demichev, C. B. Messner, S. I. Vernardis, K. S. Lilley, M. Ralser, DIA-NN: Neural networks and interference correction enable deep proteome coverage in high throughput. *Nat. Methods* **17**, 41–44 (2020).

84. A. D. Yates, P. Achuthan, W. Akanni, J. Allen, J. Allen, J. Alvarez-Jarreta, M. R. Amode, I. M. Armean, A. G. Azov, R. Bennett, J. Bhai, K. Billis, S. Boddu, J. C. Marugán, C. Cummins, C. Davidson, K. Dodiya, R. Fatima, A. Gall, C. G. Giron, L. Gil, T. Grego, L. Haggerty, E. Haskell, T. Hourlier, O. G. Izuogu, S. H. Janacek, T. Juettemann, M. Kay, I. Lavidas, T. le, D. Lemos, J. G. Martinez, T. Maurel, M. McDowall, A. McMahon, S. Mohanan, B. Moore, M. Nuhn, D. N. Oheh, A. Parker, A. Parton, M. Patricio, M. P. Sakthivel, A. I. Abdul Salam, B. M. Schmitt, H. Schuilenburg, D. Sheppard, M. Sycheva, M. Szuba, K. Taylor, A. Thormann, G. Threadgold, A. Vullo, B. Walts, A. Winterbottom, A. Zadissa, M. Chakiachvili, B. Flint, A. Frankish, S. E. Hunt, G. Ilsley, M. Kostadima, N. Langridge, J. E. Loveland, F. J. Martin, J. Morales, J. M. Mudge, M. Muffato, E. Perry, M. Ruffier, S. J. Trevanion, F. Cunningham, K. L. Howe, D. R. Zerbino, P. Flicek, Ensembl 2020. *Nucleic Acids Res.* **48**, D682–D688 (2020).

85. A. Millner, L. Running, N. Colon-Rosa, D. S. Aga, J. Frasor, G. E. Atilla-Gokcumen, Ceramide-1-phosphate is involved in therapy-induced senescence. *ACS Chem. Biol.* **17**, 822–828 (2022).

86. M. J. MacEwen, A. L. Markhard, M. Bozbeyoglu, F. Bradford, O. Goldberger, V. K. Mootha, Y. Sancak, Evolutionary divergence reveals the molecular basis of EMRE dependence of the human MCU. *Life Sci. Alliance* **3**, e202000718 (2020).

87. R. Patro, G. Duggal, M. I. Love, R. A. Irizarry, C. Kingsford, Salmon provides fast and bias-aware quantification of transcript expression. *Nat. Methods* **14**, 417–419 (2017).

88. C. Soneson, M. I. Love, M. D. Robinson, Differential analyses for RNA-seq: Transcript-level estimates improve gene-level inferences. *F1000Res* **4**, 1521 (2015).

89. M. D. Robinson, D. J. McCarthy, G. K. Smyth, edgeR: A Bioconductor package for differential expression analysis of digital gene expression data. *Bioinformatics* **26**, 139–140 (2010).

90. B. Phipson, S. Lee, I. J. Majewski, W. S. Alexander, G. K. Smyth, Robust hyperparameter estimation protects against hypervariable genes and improves power to detect differential expression. *Ann. Appl. Stat.* **10**, 946–963 (2016).

91. S. A. Stouffer, *The American Soldier. Studies in Social Psychology in World War II* (Princeton Univ. Press, 1949).

92. A. Lun. metapod: Meta-Analyses on P-Values of Differential Analyses. R package, version 1.14.0 (2024)

93. M. C. Whitlock, Combining probability from independent tests: The weighted Z-method is superior to Fisher's approach. *J. Evol. Biol.* **18**, 1368–1373 (2005).